



Cooling rates and the depth of detachment faulting at oceanic core complexes: Evidence from zircon Pb/U and (U-Th)/He ages

Craig B. Grimes

Department of Geosciences, Mississippi State University, PO Box 5448, Mississippi State, Mississippi 39762, USA (cgrimes@geosci.msstate.edu)

Michael J. Cheadle and Barbara E. John

Department of Geology and Geophysics, University of Wyoming, Laramie, Wyoming 82071, USA

Peter W. Reiners

Department of Geosciences, University of Arizona, Tucson, Arizona 85721, USA

Joseph L. Wooden

U.S. Geological Survey—Stanford Ion Microprobe Laboratory, 367 Panama Mall, Stanford, California 94305, USA

[1] Oceanic detachment faulting represents a distinct mode of seafloor spreading at slow spreading mid-ocean ridges, but many questions persist about the thermal evolution and depth of faulting. We present new Pb/U and (U-Th)/He zircon ages and combine them with magnetic anomaly ages to define the cooling histories of gabbroic crust exposed by oceanic detachment faults at three sites along the Mid-Atlantic Ridge (Ocean Drilling Program (ODP) holes 1270D and 1275D near the 15°20'N Transform, and Atlantis Massif at 30°N). Closure temperatures for the Pb/U (~800°C–850°C) and (U-Th)/He (~210°C) isotopic systems in zircon bracket acquisition of magnetic remanence, collectively providing a temperature-time history during faulting. Results indicate cooling to ~200°C in 0.3–0.5 Myr after zircon crystallization, recording time-averaged cooling rates of ~1000°C–2000°C/Myr. Assuming the footwalls were denuded along single continuous faults, differences in Pb/U and (U-Th)/He zircon ages together with independently determined slip rates allow the distance between the ~850°C and ~200°C isotherms along the fault plane to be estimated. Calculated distances are 8.4 ± 4.2 km and 5.0 ± 2.1 km from holes 1275D and 1270D and 8.4 ± 1.4 km at Atlantis Massif. Estimating an initial subsurface fault dip of 50° and a depth of 1.5 km to the 200°C isotherm leads to the prediction that the ~850°C isotherm lies ~5–7 km below seafloor at the time of faulting. These depth estimates for active fault systems are consistent with depths of microseismicity observed beneath the hypothesized detachment fault at the TAG hydrothermal field and high-temperature fault rocks recovered from many oceanic detachment faults.

Components: 16,900 words, 11 figures, 3 tables.

Keywords: Mid-Atlantic Ridge; oceanic detachment fault; oceanic core complex; thermochronometry; zircon; Ocean Drilling Program.

Index Terms: 3614 Mineralogy and Petrology: Mid-oceanic ridge processes (1032, 8416); 1140 Geochronology: Thermochronology; 8178 Tectonophysics: Tectonics and magmatism; 9325 Geographic Location: Atlantic Ocean; 1115 Geochronology: Radioisotope geochronology.

Received 12 October 2010; **Revised** 30 December 2010; **Accepted** 5 January 2011; **Published** 9 March 2011.

Grimes, C. B., M. J. Cheadle, B. E. John, P. W. Reiners, and J. L. Wooden (2011), Cooling rates and the depth of detachment faulting at oceanic core complexes: Evidence from zircon Pb/U and (U-Th)/He ages, *Geochem. Geophys. Geosyst.*, 12, Q0AG01, doi:10.1029/2010GC003391.

Theme: Oceanic Detachment Faults

Guest Editors: J. P. Canales, M. Cheadle, J. Escartin, G. Fruh-Green, and B. John

1. Introduction

[2] Along slow and ultraslow spreading mid-ocean ridges, plate separation may be accommodated by slip on long-lived, large-offset (>10 km) normal faults [e.g., *Smith et al.*, 2006; *Schroeder et al.*, 2007; *Escartin et al.*, 2008; *Cheadle and Grimes*, 2010]. These large-offset normal faults, termed oceanic detachment faults, often bound oceanic core complexes that are characterized by smooth, domal, bathymetrically high surfaces with corrugations parallel to the plate spreading direction [*Cann et al.*, 1997; *Tucholke et al.*, 1998; *Escartin et al.*, 2003; *MacLeod et al.*, 2009]. Crustal exposures denuded by detachment faults comprise substantial portions of new seafloor generated along some segments of the slow-spreading Mid-Atlantic Ridge (MAR) (>50% between 13°N and 16°N) [*Smith et al.*, 2006, 2008; *Schroeder et al.*, 2007], and the ultraslow spreading Southwest Indian Ridge (SWIR) (~40%) [*Cannat et al.*, 2006]. Crustal accretion during oceanic detachment faulting is typically highly asymmetric with respect to the ridge axis, both in terms of the crustal architecture and spreading rate [e.g., *Lagabrielle et al.*, 1998; *Allerton et al.*, 2000; *Searle et al.*, 2003; *Baines et al.*, 2008; *Grimes et al.*, 2008]. Where sampling has taken place, peridotite and gabbro are commonly recovered on the seafloor [e.g., *Cannat*, 1996; *Cann et al.*, 1997; *Karson*, 1999; *Escartin and Cannat*, 1999; *Schroeder et al.*, 2007], and ocean drilling has revealed large gabbro bodies within the footwall of several large-offset normal fault systems [*Dick et al.*, 2000; *Kelemen et al.*, 2004; *Ildfonse et al.*, 2007]. In light of these observations, it is apparent that both the nature of magmatism encountered in tectonically dominated spreading ridges, and the thickness of the crust and lithosphere is complex and yet to be fully characterized.

[3] The depths at which (1) detachment fault systems extend beneath the ridge axis and (2) gabbros within the footwall were emplaced are not well constrained, though these factors are closely related to the thermal structure of the lithosphere. The thermal structure at mid-ocean ridges is controlled

by thermal energy supplied by conduction from the mantle and intrusion of magma, and the loss of heat toward the seafloor during conduction and hydrothermal circulation. Conductive heat transfer within oceanic crust has been well described [e.g., *Sleep*, 1975], but relatively few direct constraints exist on the cumulative thermal evolution of highly extended oceanic crust. One approach to characterizing this thermal history is through the application of thermochronology using U-bearing minerals. This technique is based on the measurement of ages recorded by multiple isotopic systems with different closure temperatures, thus providing constraints on the time-temperature evolution of rocks. Thermochronometry has been utilized to study numerous large-offset fault systems in continental settings [e.g., *Foster et al.*, 1990; *John and Foster*, 1993]; however, applications to oceanic crust are limited. *John et al.* [2004] used thermochronometry to characterize the thermal history of gabbros in Ocean Drilling Program (ODP) Hole 735B at Atlantis Bank, identifying rapid cooling (time-integrated rates of >800°C/Myr from ~850°C–350°C), as well as evidence for off-axis reheating. *Schwartz et al.* [2009] followed this work to further constrain the cooling history of samples from the surface of Atlantis Bank and high-angle normal fault scarps that dissect the core complex. These workers reported similar, rapid cooling and local off-axis reheating.

[4] In this contribution, we present new Pb/U and (U-Th)/He zircon ages and use them to investigate the timing of magmatic accretion as well as subsequent cooling histories of (shallow) footwall rocks denuded during large-offset normal faulting. The integration of Pb/U and (U-Th)/He zircon ages with magnetic anomaly ages provides a comprehensive temperature-time (T-t) path over the temperature range (~850°C–200°C). Samples were collected in situ during ODP Leg 209 at 14°N–16°N, MAR, and by the submersible *Alvin* on the southern wall of Atlantis Massif (30°N, MAR). These rocks represent only the upper part of the detachment fault zone (<10–200 m below the exposed fault scarp), and likely record a different thermal history than deeper levels of oceanic core complexes. We

also compare this newly acquired data set with similar constraints reported for Atlantis Bank (SWIR) [John *et al.*, 2004; Baines *et al.*, 2009; Schwartz *et al.*, 2009]. The young age of the rocks in this study (<2.5 Ma) has the advantage of yielding smaller absolute age uncertainties, allowing higher-resolution constraints on the cooling history. These cooling histories are applied, in conjunction with independent estimates of fault slip rates, to delimit possible length scales of these fault systems while they were active, and estimate depths to the ~850°C isotherm along the fault plane, thereby allowing speculation on the original emplacement depths of rocks within the footwall and lithospheric thickness at the time of faulting. Though not previously applied in this geologic setting, this approach is essentially the inverse of techniques applied to continental fault systems in which the thermal gradient is independently known, and the thermochronometer ages of samples collected along the fault scarp are used to date the onset of denudation and subsequently determine the slip rate and active fault geometry [e.g., Foster *et al.*, 1990; John and Foster, 1993].

2. Geologic Setting

[5] Eight rock samples in this study were collected during ODP Leg 209 [Kelemen *et al.*, 2004] north and south of the fracture zone at 15°20', MAR (Figure 1). One additional sample (*Alvin* 3646-1205) was collected by submersible during the MARVEL 2000 cruise from the southern wall of the Atlantis Massif core complex adjacent to the Atlantis Transform at 30°N [Schroeder and John, 2004; Grimes *et al.*, 2008].

2.1. Fifteen-Twenty Fracture Zone

2.1.1. ODP Site 1275

[6] The seafloor at 14°N–16°N, MAR, is characterized by the absence of a well-developed, volcanic upper crust, and exposures of lower crustal gabbro and mantle peridotite are extensive on both flanks of the ridge [Rona *et al.*, 1987; Cannat *et al.*, 1992, 1997; Cannat and Casey, 1995; Lagabriele *et al.*, 1998; Kelemen *et al.*, 2004; Schroeder *et al.*, 2007; MacLeod *et al.*, 2009]. Drilling along this section of the MAR has recovered primarily mantle peridotite and gabbro [Kelemen *et al.*, 2004]. The gabbros occur as bodies with estimated sizes ranging from 10 to >150 m thick plutons (e.g., Hole 1275D), to discrete cm-scale dike or veins heavily over-

printed by deformation and low-temperature alteration (e.g., Hole 1270D) [Kelemen *et al.*, 2004; Bach *et al.*, 2004]. Radiometric dating was carried out on samples from ODP cores 1275D and 1270D.

[7] ODP Site 1275 is located at ~15°44'N, ~28 km west of the central magnetic anomaly in the axial valley (Figure 1) [Kelemen *et al.*, 2004; Schroeder *et al.*, 2007]. The deepest hole drilled during Leg 209 (1275D) was spud at the top of a domal, bathymetric high interpreted to be an oceanic core complex [Escartín and Cannat, 1999; MacLeod *et al.*, 2002; Escartín *et al.*, 2003; Fujiwara *et al.*, 2003; Kelemen *et al.*, 2004]. At this location the seafloor is smooth, with ridge-perpendicular corrugations (Figure 1). Seabed rock drilling (<1 m long cores) on the surface of this core complex recovered extensive fault rocks, providing strong evidence that it represents a fault surface [MacLeod *et al.*, 2002; Escartín *et al.*, 2003]. Hole 1275D was drilled ~14 km east of the inferred breakaway (Figure 1d) and penetrated 209 m below the seafloor (mbsf) into the footwall to the detachment fault (total recovery = 50%). The upper ~50 m of core consists primarily of ultramafic rock types with minor diabase [Kelemen *et al.*, 2004]. The lower ~160 m is composed of gabbroic rocks intruded by diabase, plagiogranite, and other gabbroic units. Recovered proportions for the entire core include 74% gabbro (including gabbro, gabbro-norite, Fe-Ti oxide gabbro, Fe-Ti oxide gabbro-norite, and minor olivine gabbro), 14% ultramafic rocks, 10% diabase, and 2% plagiogranite (Figure 2). Numerous igneous contacts within the core imply that the gabbroic section was built by multiple intrusive events [Kelemen *et al.*, 2004]. Semibrittle and brittle deformation is extensive in the upper 30 m [Schroeder *et al.*, 2007]. At depths greater than 50 mbsf, the core records very little deformation, and alteration occurred largely under static conditions [Kelemen *et al.*, 2004].

[8] In total, 6 rock samples from core 1275D were dated. Five samples comprised cm-scale plagiogranite dikes intruding gabbro, spanning 10–200 mbsf (Figures 3a–3c). An additional sample at 167 mbsf (Figure 3d) was collected from a complex interval ~3.3 m thick that includes Fe-Ti oxide gabbro and olivine-bearing microgabbro hosting diorite xenoliths, intermingled with quartz diorite-tonalite. Upper and lower contacts with medium to coarse-grained Fe-Ti oxide gabbro are reported in the core, but the relative age relationships were difficult to discern [Kelemen *et al.*, 2004].

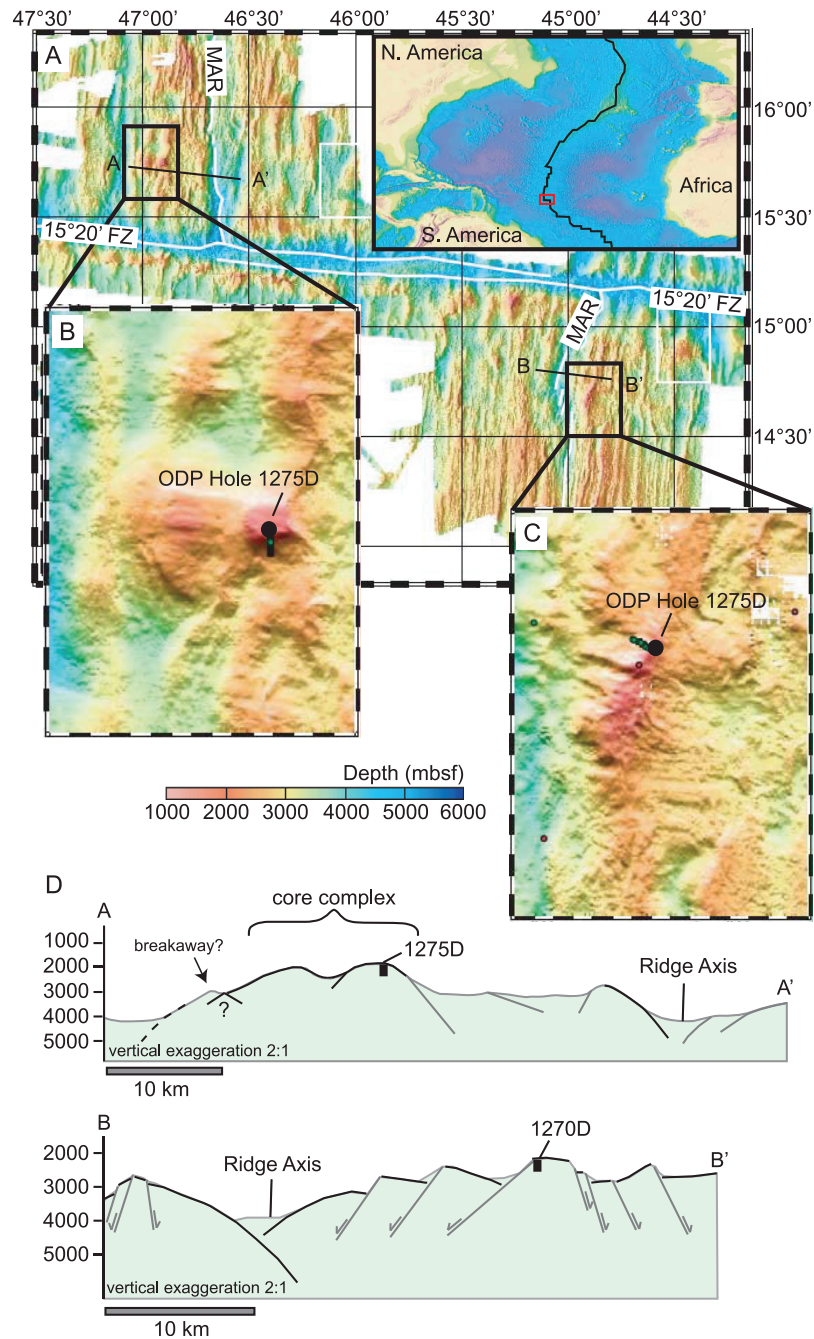


Figure 1. (a) Seabeam bathymetric map of the region surrounding the 15°20' Fracture Zone, MAR (modified from Fujiwara *et al.* [2003]). (b) Blowup of the bathymetry at ODP Site 1275; note the spreading direction parallel corrugations on the surface of the smooth, domal, bathymetric high or core complex (modified from Fujiwara *et al.* [2003]). (c) Blowup of the bathymetry at ODP Site 1270 (modified from Fujiwara *et al.* [2003]). (d) Bathymetric profiles along cross-section lines A-A' and B-B' (shown in Figure 1a). Nonfaulted seafloor shown as gray line; inferred faults shown as black lines (A-A' modified from Escartín *et al.*, 2003; B-B' modified from Schroeder *et al.* [2007]).

[9] The small-volume plagiogranites occur throughout the core, and are interpreted to represent some of the latest melts to crystallize. They typically comprise plagioclase + amphibole ± quartz ± Fe-Ti oxide ± alkali feldspar ± zircon ± apatite.

Contacts between the plagiogranite dikes and host gabbro range from sharp to completely gradational (Figures 3a–3c), and locally exhibit complex mingling relationships [Kelemen *et al.*, 2004]. Contacts showing mingling with the wall rock imply that

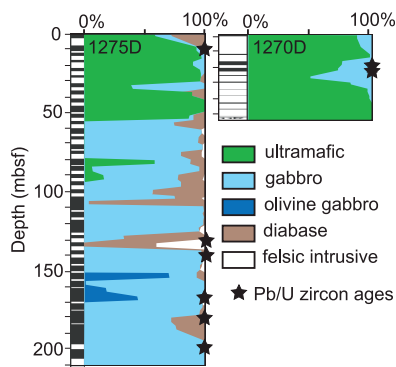


Figure 2. Columns depicting rock types recovered versus depth in ODP cores 1270D and 1275D normalized to percent of recovery. The recovered rock types are averaged over 10 m intervals and normalized to 100%, and a given 10 m interval typically comprises more than one rock type. The actual percentage of rock recovered over each interval is represented by the black fill in the left-hand column of both plots (modified from *Kelemen et al.* [2004]). Stars indicate plots of zircon-bearing samples analyzed in this study.

the intrusion of at least some of the plagiogranite dikes occurred while earlier gabbros were above the solidus. These observations are particularly relevant for interpreting age and cooling information recorded by the plagiogranite dikes and applying the chronologic data to the gabbroic section as a whole, as they imply a relatively short time interval between emplacement of the gabbroic section and formation of zircon-saturated felsic melts.

[10] Similar evolved dikes and veins recovered from the predominantly gabbroic crustal sections recovered in ODP core 735B and IODP core U1309D have estimated emplacement temperatures $>750^{\circ}\text{C}$ – 800°C [*Robinson et al.*, 2002; *Blackman et al.*, 2006]. Direct constraints from Ti-in-zircon thermometry applied to normal magmatic zircons from plagiogranite yields crystallization temperatures ranging from 680°C to 850°C (average $750^{\circ}\text{C} \pm 90^{\circ}\text{C}$, 2σ) [*Grimes et al.*, 2009], which are below the estimated solidus for MAR gabbros ($860^{\circ}\text{C} \pm 30^{\circ}\text{C}$) [*Coogan et al.*, 2001]. Multiple origins have been proposed for these plagiogranite dikes, including differentiation by $\sim 85\%$ – 90% fractional crystallization of basaltic magma [*Niu et al.*, 2002], liquid immiscibility in late stage, iron-rich melts [*Natland et al.*, 1991], and anatexis of hydrated crustal gabbros at temperatures $>900^{\circ}\text{C}$ [*Koepke et al.*, 2007]. *Kelemen et al.* [2004] initially hypothesized that the plagiogranite dikes in core 1275D represent small volumes of highly evolved melt extracted from the gabbros during late-stage crystallization. This interpretation

is supported by mantle-like $\delta^{18}\text{O}$ (zircon) values reported for these samples [*Grimes et al.*, 2010]. Regardless of the origin, a thermal pulse related to the intrusion of gabbroic magma is required to form the plagiogranites, and the Pb/U zircon age reflects timing of the near-solidus (rather than liquidus) temperatures of that magma.

2.1.2. ODP Site 1270

[11] Site 1270 is located at $14^{\circ}43'\text{N}$, ~ 15 km east of the central magnetic anomaly along the MAR [*Fujiwara et al.*, 2003] (Figure 1). The site is on a gently west dipping ($\sim 10^{\circ}$), striated, laterally continuous surface interpreted as a large displacement fault scarp [*Schroeder et al.*, 2007]. The seafloor is also cut by steeper, secondary faults (Figure 1). Unlike Site 1275, faulting did not result in formation of a domal core complex, although this location has been described as a “corrugated megamullion structure” [*Fujiwara et al.*, 2003]. Previous sampling by submersible, as well as drilling on ODP Leg 209 recovered dominantly peridotite, with gabbro and minor basalt and diabase [*Kelemen et al.*, 1998; *Fujiwara et al.*, 2003, Figure 2; *Schroeder et al.*, 2007]. All holes drilled at Site 1270 are characterized by low recovery, and fault gouge was frequently encountered at 15–20 m depth. The total depth penetrated by Hole 1270D was 57 mbsf, with 7.7 m of rock recovered comprising 91% harzburgite, 7% dunite, and 2% gabbroic dikes (Figure 2) [*Kelemen et al.*, 2004]. The dikes are 1–2 cm thick, highly altered, and preserve evidence of highly localized, synkinematic, high-temperature alteration [*Bach et al.*, 2004; *Jöns et al.*, 2009]. Relict igneous minerals are sparse, but locally include plagioclase, clinopyroxene, amphibole, Fe-Ti oxide minerals, zircon and apatite. Mantle-like $\delta^{18}\text{O}$ confirm an igneous origin for the zircons [*Grimes et al.*, 2010]. Plagioclase is almost completely replaced; brown amphibole replaces clinopyroxene locally adjacent to contacts with peridotite. Based on geochemical modeling, as well as the presence of zircon and apatite, *Jöns et al.* [2009] concluded these dikes were likely altered plagiogranite intrusions. Approximately 230 m to the west and downslope along the fault scarp, Hole 1270B penetrated 46 mbsf and 98% gabbroic rock types were recovered, including evolved gabbro and gabbro-norite containing Fe-Ti oxide minerals. It is possible that the dikes intruding peridotite in core 1270D originated as differentiated liquids that migrated away from these thicker gabbros during crystallization and compaction [*Kelemen et al.*, 2004].

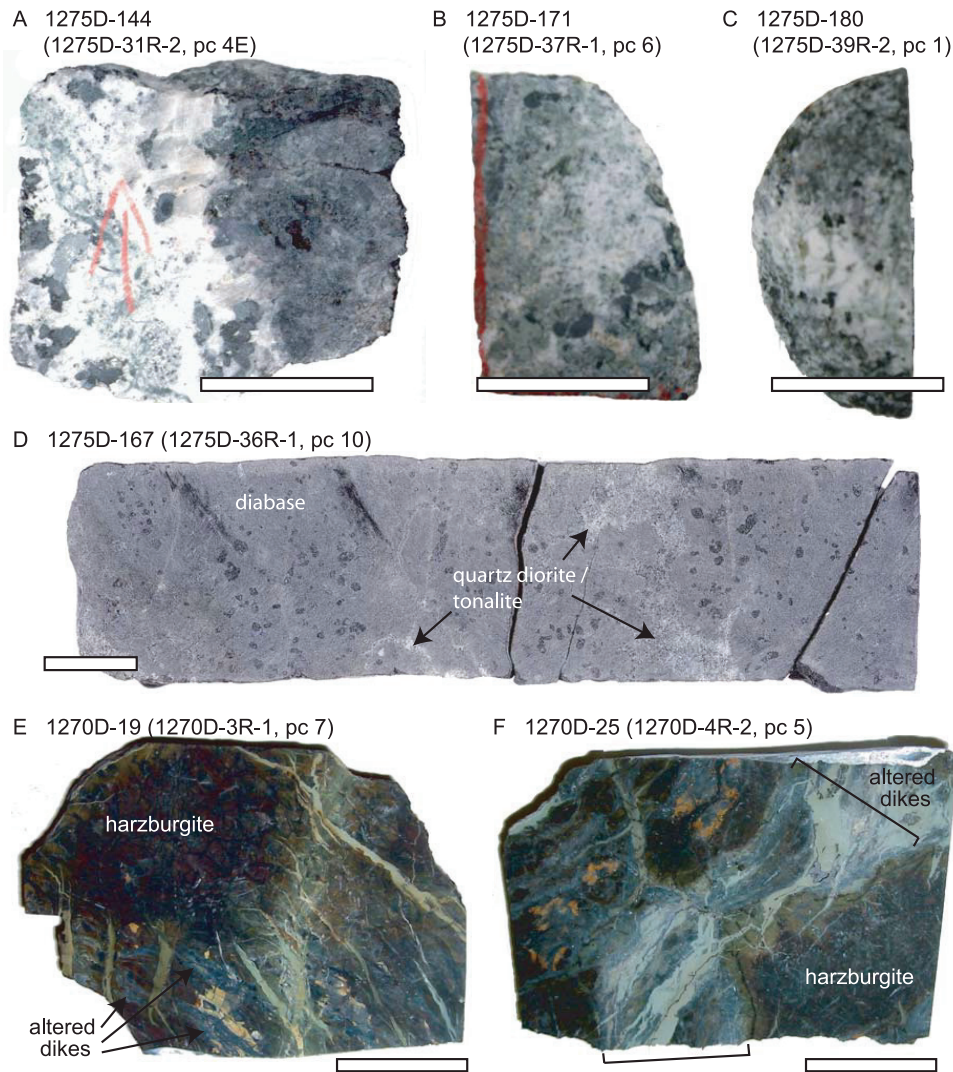


Figure 3. Representative rock types host to zircons. (a–c) Felsic dikes. (d) Olivine and plagioclase phyric diabase intermingled with felsic patches (courtesy of ODP Leg 209 Report by *Kelemen et al.* [2004]). (e–f) Centimeter-scale greenschist-grade shear zones or dikes (dominantly chlorite-actinolite or tremolite schist) intruding peridotite. Scale bars are 2 cm.

[12] The thin dikes intruding peridotite in 1270D are inferred to have been emplaced while the peridotite was at temperatures $>600^{\circ}\text{C}$ [*Kelemen et al.*, 2004; *Bach et al.*, 2004; *Schroeder et al.*, 2007], based on intimate interfingering of gabbro into the host peridotite, high-temperature contacts (e.g., coarse grain size at the contacts), and ductile fabrics locally within the dikes. Gabbro recovered in the upper 10–15 m of 1270B show extensive ductile, as well as minor brittle, deformation that may be in part related to movement along the planar fault surface exposed on the seafloor [*Kelemen et al.*, 2004].

[13] Paleomagnetic data imply tectonic rotations of $\sim 60^{\circ}$ – 80° at both sites (ODP holes 1270D and

1275D) [*Kelemen et al.*, 2004; *Garces and Gee*, 2007]. This interpretation is based on inclination of the magnetic remanence vector in core recovered during drilling that are shallower than expected for the geocentric axial dipole (GAD) at this latitude, and the assumption that the rotation occurs about a horizontal axes parallel to the ridge axis. This latter assumption is supported by fully reoriented core and paleomagnetic observations from Atlantis Massif at 30°N on the MAR, which constrain the rotation axis to be parallel to the ridge axis at that core complex [*Morris et al.*, 2009]. Given the present interpretation of large rotations, the paleovertical section actually sampled by the drill cores would have been significantly shorter (i.e., 35–100 m for Hole 1275D).

2.1.3. Paleomagnetic Constraints on Crustal Age

[14] The age of the crust penetrated by drilling during ODP Leg 209 can be estimated from sea surface magnetic anomalies [Fujiwara *et al.*, 2003]. Continuous downhole magnetic measurements collected during ODP Leg 209 [Kelemen *et al.*, 2004; Garces and Gee, 2007] provide more detailed measurements of the local magnetic polarity. The ages inferred from magnetic anomaly data correspond to either cooling through the Curie temperature or the formation of magnetic minerals during serpentinization. The Curie temperature of magnetite in gabbro is $<580^{\circ}\text{C}$ [Tarling, 1983], whereas the temperature of magnetite formation during serpentinization near the $15^{\circ}20'$ Fracture Zone is estimated to have begun $\sim 350^{\circ}\text{C}$ and continued below 250°C [Bach *et al.*, 2004]. Magnetization is a continuous process, and can be acquired over a range of temperatures [e.g., Gee and Meurer, 2002]. In the following discussion, we therefore assume remanence was acquired at $530^{\circ}\text{C} \pm 50^{\circ}\text{C}$ for gabbroic rocks, and $300^{\circ}\text{C} \pm 50^{\circ}\text{C}$ for peridotite.

[15] Shipboard magnetic measurements made during ODP Leg 209 indicate that gabbros from core 1275D are reversely magnetized [Kelemen *et al.*, 2004; Garces and Gee, 2007]. Sea surface magnetic anomaly data are consistent with this observation, and suggest that the remanence was acquired during chron C2r (1.95–2.58 Ma) [Ogg and Smith, 2004]. Hole 1275D was spud east of the peak of the anomaly [cf. Fujiwara *et al.*, 2003], implying that it is younger than the midpoint of chron C2r; we therefore refine the magnetic age estimate to between 1.95 and 2.26 Ma ($\sim 2.11 \pm 0.16$ Ma). With this magnetic age, the position of Hole 1275D 28 km off-axis yields a time-integrated spreading rate of ~ 13.3 mm/yr that is consistent with the regional half-spreading rate over the last 5 Ma (13 mm/yr) [Fujiwara *et al.*, 2003].

[16] Determining the magnetic polarity at Site 1270 is complicated by subhorizontal magnetic inclinations measured for both gabbroic rocks from core 1270B and serpentinized peridotite from core 1270D (<230 m east of 1270B) [Kelemen *et al.*, 2004]. Based on comparisons of the foliation orientation with the remanence directions, Garces and Gee [2007] concluded that the gabbros are reversely magnetized and peridotites have normal polarity. These conclusions are consistent with the location of Site 1270 near the boundary of the broad region of normal magnetization flanking the present-day ridge axis [Fujiwara *et al.*, 2003; Garces and Gee, 2007]

that may include crust generated during the Jaramillo (C1r.1n), Bruhnes (C1n), and the intervening reversed polarity interval C1r.1r [Garces and Gee, 2007]. The normal polarity of 1270D peridotites is unlikely to be the result of a viscous remanent magnetization imparted by exposure to the current normal polarity field, because their shallow inclinations imply a similar magnitude of rotation since acquisition of remanence as the gabbro sampled in 1270B [Kelemen *et al.*, 2004; Garces and Gee, 2007]. Magnetic remanence hosted by the peridotites was therefore most likely acquired in magnetite formed during serpentinization of olivine ($<350^{\circ}\text{C}$) [Bach *et al.*, 2004]. The magnetic polarities of gabbro and peridotite at Site 1270 therefore bracket a magnetic reversal (reversed to normal), providing additional constraints on the age and cooling history of these rocks. For gabbros from 1270B, the observations suggest that remanence was acquired either during chron C1r.1r (0.78–0.99 Ma) [Ogg and Smith, 2004], or before the start of the Jaramillo (>1.07 Ma) [Ogg and Smith, 2004]. The normally magnetized peridotite would reflect later, lower temperature magnetization either during the Jaramillo (0.99–1.07 Ma) [Ogg and Smith, 2004] or the Bruhnes (<0.78 Ma) [Ogg and Smith, 2004] normal polarity chron. Low amplitude and discontinuous negative polarities are observed in the sea surface anomaly data to the west and southwest of Site 1270 that likely represent subchron C1r.1r [cf. Fujiwara *et al.*, 2003]. Based on this observation we favor the interpretation that the gabbros were emplaced and magnetized prior to the Jaramillo (>1.07 Ma), followed by magnetization of the peridotites during the Jaramillo (1.03 ± 0.04 Ma). The geochronologic data presented here support such an interpretation. The estimated age of the gabbros based on magnetic constraints along with the distance off-axis of ~ 15 km loosely constrains the time-integrated spreading rate to have been <14 km/Myr, and is consistent with the regional half-spreading rate over the past 5 Ma of 12.8 km/Myr [Fujiwara *et al.*, 2003].

2.2. The Atlantis Massif Sample Site

[17] Atlantis Massif is a well-studied oceanic core complex bounded by a detachment fault located at 30°N on the Mid-Atlantic Ridge [Cann *et al.*, 1997; Blackman *et al.*, 2002; Karson *et al.*, 2006]. Mapping surveys and sampling of Atlantis Massif has been carried out along the southern wall, the surface of the central dome, and during IODP drilling on the central dome (IODP Hole U1309D). A detachment fault shear zone extends at least 100 m below the top

of the southern wall adjacent to the Atlantis Transform, and is characterized by strongly foliated to mylonitic serpentinites and talc-amphibole schists [e.g., *Schroeder and John*, 2004; *Karson et al.*, 2006]. In contrast, core recovered from Hole U1309D from the central dome included dominantly gabbroic rock types, with notably minor amounts of ultramafic rocks [*Blackman et al.*, 2006]. Fully reoriented core taken with paleomagnetic inclination data from IODP Hole U1039D imply $46^\circ \pm 6^\circ$ counterclockwise rotation below 580°C [*Morris et al.*, 2009], providing a minimum estimate for the dip on the fault at initiation. The regional symmetric half spreading rate at this latitude is ~ 12 mm/yr. However, Pb/U zircon ages indicate that the Atlantis Massif core complex formed during a short-lived period of spreading asymmetry, with between 70 and 100% of the plate motion accommodated by detachment faulting west of the ridge [*Grimes et al.*, 2008]. Spreading asymmetry of 60%–80% of the full rate has been demonstrated during formation of several other core complexes on the basis of Pb/U zircon ages and magnetic anomalies, including the Kane oceanic core complex [*Cheadle et al.*, 2008], Atlantis Bank [*Baines et al.*, 2008], and Fuji Dome [*Searle et al.*, 2003]. Based on the Pb/U zircon ages from the southern wall of Atlantis Massif, we use an intermediate time-integrated spreading rate of 20 mm/yr since emplacement (80% asymmetric) in the following discussions.

[18] One rock sample from Atlantis Massif is incorporated by this study. Sample 3646-1205 is a talc-amphibole-chlorite schist collected from the southern wall of Atlantis Massif, at an inferred depth of 37 m structurally below the detachment fault surface [*Schroeder and John*, 2004], and has a previously reported $^{206}\text{Pb}/^{238}\text{U}$ zircon age of 1.07 ± 0.03 Ma [*Grimes et al.*, 2008]. Sample 3646-1205 was collected along the south wall in a broad region of normal polarity magnetization [*Gee and Blackman*, 2004], however, magnetic anomaly boundaries are difficult to resolve along the wall and no magnetic age has been assigned.

3. Analytical Methods and Results

3.1. Sampling and Mineral Separation

[19] Thirteen samples of quartz diorite to tonalite (i.e., ‘plagiogranite’) from holes 1275D and 1270D were processed for zircon separation; zircons were recovered from eleven of these. Sample volumes available for crushing ranged from 30 to 100 cc. To separate zircons, rocks were first coarse crushed by

hand and reduced to <300 μm particle size using a disc mill pulverizer. Magnetic minerals were removed using a Frantz magnetic separator, and remaining material was run through a single heavy liquid step using diiodomethane to concentrate zircon. Zircon yields were variable, and tens to hundreds of grains were commonly recovered.

3.2. U-Pb Analyses

3.2.1. Analytical Methods

[20] U-Pb dating was carried out at the USGS–Stanford Ion Microprobe Facility using the sensitive high-resolution ion microprobe–reverse geometry (SHRIMP-RG). Zircon standard R33 served as the $^{206}\text{Pb}/^{238}\text{U}$ age standard and zircon standard CZ3 was used to calibrate U concentrations. Prior to analysis, all samples were imaged using reflected light, and cathodoluminescence to avoid cracks, inclusions, and pitted areas. Details of sample preparation, analytical setup, data reduction, and age corrections are discussed by *Grimes et al.* [2008] and followed the procedures described by *Williams* [1998]. A correction for initial ^{238}U – ^{230}Th secular disequilibrium was applied using the equations of *Parrish and Noble* [2003], assuming initial Th/U = 3 for the parent magma (average value for MORB from the northern MAR). The correction increases measured ages by 3.3%–9.4% depending on measured Th/U in single zircons.

[21] The possibility exists that variation in the spot ages from a given rock sample is not due solely to normally distributed analytical error, and may reflect geologic variation due to crystallization of zircon during cooling [e.g., *Lissenberg et al.*, 2009], and/or minor amounts of Pb loss. Tests for whether the spot ages for each sample are normally distributed were carried out following the methods of *Baines et al.* [2009, supplementary material], and indicate that the spread in the data from each sample are consistent with a normal distribution. Sample ages have thus been calculated as weighted averages of the spot analyses using ^{207}Pb and ^{230}Th corrected isotopic ratios (typically 6–12 spots per rock sample). However, it cannot be ruled out that geologic events occurring over timescales shorter than the quoted uncertainties have taken place. In particular, zircons within a rock may have crystallized over an age range corresponding to cooling through a temperature range of perhaps $\sim 150^\circ\text{C}$ or less [*Grimes et al.*, 2009]. As long as the cooling rate corresponding to this age range is not anomalous and is consistent with the overall cooling rate



from $\sim 850^{\circ}\text{C}$ to 200°C , then such age variation would not alter the conclusions presented here.

[22] The nominal closure temperature of Pb diffusion in zircon is $>900^{\circ}\text{C}$ [Cherniak and Watson, 2003]. However, formation temperatures of plagiogranite host rocks estimated from plagioclase-amphibole thermometry, and Ti-in-zircon thermometry indicate that zircon crystallization to lower temperatures is not uncommon in this setting [e.g., Robinson *et al.*, 2002] (see discussion by Grimes *et al.* [2009]). Thus, crystallization temperatures are more appropriate estimate of the temperature to which the Pb/U age corresponds. Measured Ti concentrations and Ti-in-zircon temperatures are reported by Grimes *et al.* [2009], and have been calculated using the recalibrated Ti-in-zircon thermometer [Watson and Harrison, 2005] of Ferry and Watson [2007] assuming a Ti activity = 0.7, Si activity = 1, and $P = 2$ kbars. Assuming these correction factors, corrected values are within 5°C – 10°C of the uncorrected values. Zircons in this study yield comparable corrected Ti-in-zircon temperatures, averaging $\sim 820^{\circ}\text{C} \pm 60^{\circ}\text{C}$ (2σ , $n = 7$) for core 1275D, $\sim 830^{\circ}\text{C} \pm 40^{\circ}\text{C}$ (2σ , $n = 12$) for core 1270D, and $\sim 850^{\circ}\text{C} \pm 50^{\circ}\text{C}$ (2σ , $n = 5$) for sample 3646-1205.

3.2.2. Results From Hole 1275D

[23] Ages were determined for six rocks from core 1275D. The uncorrected U-Pb isotopic data are plotted on Tera and Wasserburg concordia diagrams [Tera and Wasserburg, 1972] in Figure 4 and listed in Table 1. The concordia diagrams are used for visual inspection and assessment of coherent age groups, but have not been used to determine an age. All quoted ages are ^{207}Pb and ^{230}Th corrected $^{206}\text{Pb}/^{238}\text{U}$ weighted average ages determined from multiple single-grain analyses per rock sample (Figure 5). The weighted average age errors are given at 95% confidence, and were calculated using Isoplot v. 3.00 [Ludwig, 2003]. Five of the 6 rock samples dated (excluding 1275D-167) give zircon ages ranging from 2.12 ± 0.17 to 2.31 ± 0.10 Ma, which are indistinguishable given the measurement uncertainties. Taking a weighted average of these 5 rock ages, the average accretion age of this crustal section is taken to be 2.22 ± 0.10 Ma (mean square of weighted deviates (MSWD) = 1.6). However, the entire section was not emplaced during a single magmatic event. Igneous contacts within the core indicate that this short crustal section was constructed by numerous intrusive pulses [e.g., Kelemen *et al.*, 2004]. Additionally, sample 1275D-167 yields an age of 2.40 ± 0.11 Ma that is not

within error of the nearby sample at 180 mbsf (2.19 ± 0.09 Ma; Figure 5). Considering these age differences (and associated errors) between the youngest and oldest samples, the zircon ages delimit the period of accretion to no less than 40 kyr.

3.2.3. Results From Hole 1270D

[24] Zircon ages were determined for rock samples at 19 and 25 mbsf in core 1270D (Figure 6). Ten zircons from 1270D-19 were dated, although five of these grains contained appreciable amounts of common lead ($>30\%$ f_{206} ; Table 1) and correspondingly have large errors (Figure 6). If all ten age spots are included, the weighted average age for sample 1270D-19 is 1.27 ± 0.04 Ma (MSWD = 1.4). Excluding the spot analyses with $>30\%$ f_{206} , the weighted average determined from the remaining 5 spots yields a statistically equivalent age of 1.28 ± 0.03 and a slightly lower MSWD = 1.1. Twelve zircons from 1270D-25 were dated. Including all spot analyses, the weighted mean age for this rock sample is 1.13 ± 0.05 Ma (MSWD = 1.2). Excluding three grains with $>30\%$ f_{206} once again has little effect on the calculated age, yielding a weighted average of 1.14 ± 0.04 Ma with the lower MSWD = 0.72. The ages quoted in the following discussion were calculated by excluding spot analyses having $>30\%$ f_{206} . Inclusion of these less reliable data however, would not impact any conclusions drawn from the age data. Considering the uncertainties, the zircon ages imply episodic dike intrusion spanning a minimum of ~ 70 kyr.

3.3. (U-Th)/He Analyses

3.3.1. Analytical Methods

[25] The (U-Th)/He ages presented here were measured at Yale University following procedures described by Reiners [2005]. Helium was extracted from single crystals of zircon by Nd-YAG laser heating, and measured on a stable isotope quadrupole mass spectrometer. U and Th isotopic compositions were determined by Parr bomb dissolution and solution ICP-MS. Zircon in this study had mean weighted average radii of 46 to $74 \mu\text{m}$ (Table 2). The α ejection correction was applied to all raw (U-Th)/He ages following the approach of Farley *et al.* [1996], modified for the tetragonal prism morphology and density of zircon [Reiners, 2005]. Uncertainties on the individual (U-Th)/He ages discussed are reported at the 2σ level based on the

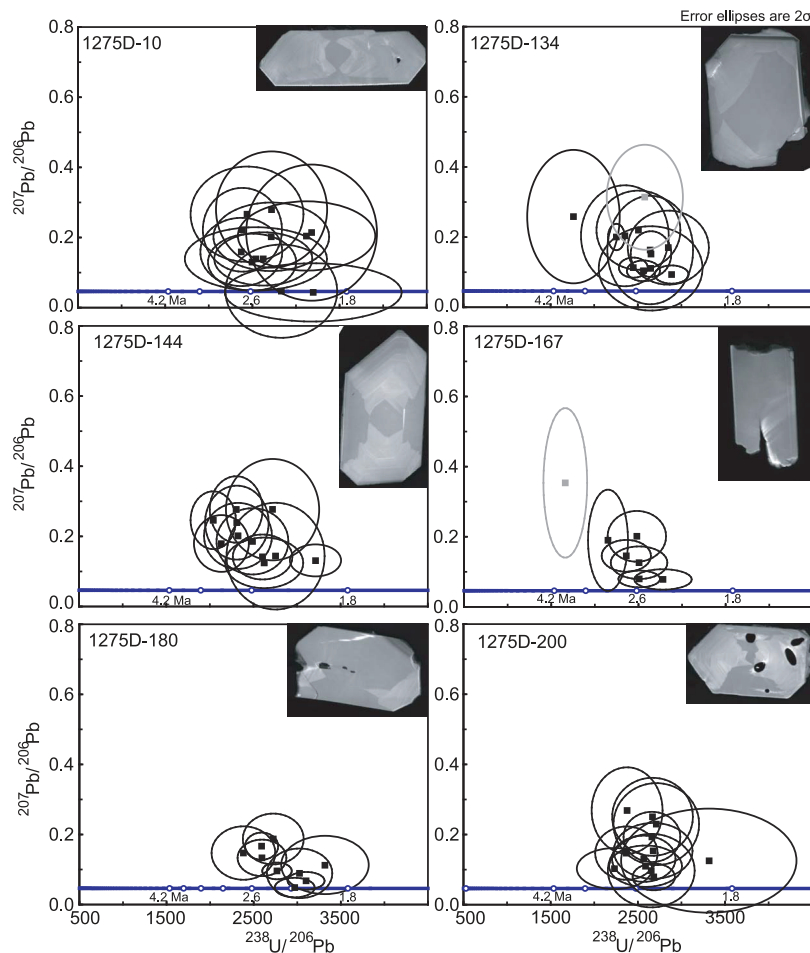


Figure 4. *Tera and Wasserburg* [1972] concordia plots for zircons analyzed from ODP core 1275D (15°44'N, MAR) by SHRIMP-RG. The bold line near the bottom of each plot represents concordia (open circles indicate reference ages). Errors on spot analyses are 2σ . Spot analyses for most sample populations cluster on or near concordia or are pulled off of concordia along a linear array reflecting mixing with a small component of initial common lead. Gray error ellipses indicate spot analyses with $>30\%$ f_{206} , which have been rejected when determining weighted average ages. These diagrams are shown for visualization purposes only and were not used to determine an age (see Figure 5 for ^{207}Pb - ^{230}Th corrected ages).

reproducibility of the zircon standard ($\pm 9\%$, 2σ) [Reiners, 2005].

[26] Estimated closure temperatures for the (U-Th)/He system in zircons vary slightly depending on grain size and rate of cooling (see Dodson [1973] for a general discussion on closure temperature). Diffusion parameters have been experimentally determined for zircon by Reiners *et al.* [2004], and yield a nominal closure temperature of $\sim 180^\circ\text{C}$ assuming an effective grain radius of $60\ \mu\text{m}$ and a cooling rate of $10^\circ\text{C}/\text{Myr}$. Calculated and predicted cooling rates for lower oceanic crust range from 10^1°C to $10^5^\circ\text{C}/\text{Myr}$ depending on the temperature range investigated [Coogan *et al.*, 2002; John *et al.*, 2004; Maclennan *et al.*, 2005; VanTongeren *et al.*, 2008; Schwartz *et al.*, 2009]. Cooling rates esti-

mated at temperatures $<400^\circ\text{C}$ are $\sim 10^2^\circ\text{C}/\text{Myr}$ [John *et al.*, 2004; Meurer and Gee, 2002]. For a cooling rate of rate of $100^\circ\text{C}/\text{Myr}$ and assuming the diffusion parameters of Reiners *et al.* [2004], we calculate a closure temperature of 207°C for zircons with the mean radius of 60 microns (average radius of zircons in this study). An average closure temperature of $\sim 210^\circ\text{C} \pm 15^\circ\text{C}$ is used in the following discussion, similar to the closure temperature used by Schwartz *et al.* [2009]. The error quoted on the closure temperature is largely a function of the uncertainty in cooling rate.

3.3.2. Results From Core 1275D

[27] The (U-Th)/He age of four zircons from core 1275D was determined. Three of these grains (from



Table 1. SHRIMP Pb/U Isotope Analysis of Zircons From 14°N–16°N, MAR

Grain Sample	Concentrations				Atomic Ratios ^a		207Pb Corrected		207Pb Corrected Ages (Ma)		207Pb and 230Th Corrected Ages	
	U (ppm)	Th (ppm)	206Pb ^b (ppm)	f ₂₀₆ ^c (%)	238U/206Pb ^d (abs err)	207Pb/206Pb ^d (abs err)	206Pb/238U ^e (abs err)	206Pb/238U ^f (1σ)	Weighted Average Age	206Pb/238U ^e (abs err)	206Pb/238U ^f (2σ)	Weighted Average Age
<i>ODP Hole 1275D: 75D-10, Brecciated Plagiogranite</i>												
1.1	19	12	0.007	27.57	2438.7 ± 264.5	0.0838 ± 0.0127	0.00030 ± 0.00005	1.91 ± 0.29	2.03 ± 0.18	0.00031 ± 0.00009	2.00 ± 0.58	2.12 ± 0.18
1.2	33	21	0.012	14.10	2372.8 ± 191.8	0.0690 ± 0.0075	0.00036 ± 0.00004	2.33 ± 0.24	MSWD = 1.2	0.00038 ± 0.00007	2.42 ± 0.47	MSWD = 1.2
1.3	27	16	0.007	19.77	3119.8 ± 322.5	0.0492 ± 0.0034	0.00026 ± 0.00003	1.66 ± 0.21		0.00027 ± 0.00006	1.74 ± 0.41	
1.4	32	19	0.010	11.61	2625.1 ± 229.8	0.0518 ± 0.0047	0.00034 ± 0.00003	2.17 ± 0.22		0.00035 ± 0.00007	2.26 ± 0.43	
1.5	35	24	0.009	21.03	3179.5 ± 306.8	0.0642 ± 0.0042	0.00025 ± 0.00004	1.60 ± 0.26		0.00026 ± 0.00008	1.68 ± 0.52	
1.6	38	18	0.012	10.10	2832.3 ± 261.8	0.0567 ± 0.0070	0.00035 ± 0.00004	2.27 ± 0.26		0.00037 ± 0.00008	2.37 ± 0.52	
1.7	29	18	0.009	29.19	2720.1 ± 260.4	0.1889 ± 0.0239	0.00026 ± 0.00004	1.68 ± 0.27		0.00027 ± 0.00008	1.76 ± 0.54	
1.8	36	24	0.012	10.46	2496.6 ± 206.4	0.0662 ± 0.0062	0.00036 ± 0.00003	2.31 ± 0.22		0.00037 ± 0.00007	2.40 ± 0.44	
1.9	28	16	0.008	11.20	3198.2 ± 414.4	0.0603 ± 0.0053	0.00035 ± 0.00005	2.24 ± 0.30		0.00036 ± 0.00009	2.33 ± 0.61	
1.10	37	25	0.013	11.62	2540.7 ± 333.0	0.1956 ± 0.0085	0.00035 ± 0.00005	2.24 ± 0.32		0.00036 ± 0.00010	2.33 ± 0.64	
1.11	34	20	0.012	22.01	2385.4 ± 185.3	0.0580 ± 0.0041	0.00033 ± 0.00004	2.11 ± 0.24		0.00034 ± 0.00008	2.20 ± 0.49	
1.12	23	15	0.007	19.52	2716.8 ± 271.1	0.6201 ± 0.0185	0.00030 ± 0.00004	1.91 ± 0.23		0.00031 ± 0.00007	1.99 ± 0.46	
<i>ODP Hole 1275D: 75D-134, Plagiogranite Dike</i>												
1.1	40	21	0.013	8.10	2647.7 ± 243.2	0.0838 ± 0.0127	0.00035 ± 0.00004	2.24 ± 0.26	2.23 ± 0.10	0.00036 ± 0.00008	2.33 ± 0.51	2.31 ± 0.10
1.2	266	153	0.089	7.23	2565.8 ± 77.5	0.0690 ± 0.0075	0.00036 ± 0.00001	2.33 ± 0.08	MSWD = 1.7	0.00038 ± 0.00003	2.42 ± 0.17	MSWD = 1.7
1.3	57	29	0.017	15.51	2850.3 ± 190.0	0.0492 ± 0.0034	0.00030 ± 0.00003	1.91 ± 0.18		0.00031 ± 0.00006	2.00 ± 0.36	
1.4	16	7	0.008	26.58	1762.1 ± 216.7	0.0518 ± 0.0047	0.00042 ± 0.00008	2.69 ± 0.50		0.00043 ± 0.00016	2.78 ± 1.00	
1.5	48	26	0.016	33.54	2579.9 ± 178.1	0.0642 ± 0.0042	0.00026 ± 0.00004	1.66 ± 0.25		0.00027 ± 0.00008	1.75 ± 0.49	
1.6	195	104	0.063	13.21	2651.7 ± 95.1	0.0567 ± 0.0070	0.00033 ± 0.00002	2.11 ± 0.12		0.00034 ± 0.00004	2.20 ± 0.24	
1.7	360	241	0.126	8.36	2448.7 ± 67.5	0.1889 ± 0.0239	0.00037 ± 0.00001	2.41 ± 0.08		0.00039 ± 0.00003	2.50 ± 0.16	
1.8	689	479	0.263	19.30	2254.9 ± 39.3	0.0662 ± 0.0062	0.00036 ± 0.00002	2.31 ± 0.10		0.00037 ± 0.00003	2.39 ± 0.19	
1.9	39	22	0.013	21.74	2507.5 ± 196.5	0.0603 ± 0.0053	0.00031 ± 0.00004	2.01 ± 0.23		0.00033 ± 0.00007	2.10 ± 0.45	
1.10	361	230	0.107	5.91	2888.1 ± 79.4	0.1956 ± 0.0085	0.00033 ± 0.00001	2.10 ± 0.07		0.00034 ± 0.00002	2.19 ± 0.13	
1.11	42	22	0.014	14.66	2642.6 ± 200.9	0.0580 ± 0.0041	0.00032 ± 0.00004	2.08 ± 0.25		0.00034 ± 0.00008	2.17 ± 0.51	
1.12	29	16	0.011	19.74	2352.2 ± 205.7	0.6201 ± 0.0185	0.00034 ± 0.00004	2.20 ± 0.29		0.00035 ± 0.00009	2.29 ± 0.57	
<i>ODP Hole 1275D: 75D-144, Plagiogranite Dike in Oxide-Bearing Gabbro</i>												
1.1	50	31	0.016	9.80	2623.0 ± 19.6	0.0476 ± 0.0075	0.00034 ± 0.00003	2.22 ± 0.18	2.04 ± 0.17	0.00036 ± 0.00006	2.30 ± 0.36	2.12 ± 0.17
2.1	78	43	0.033	25.02	2038.4 ± 106.1	0.0527 ± 0.0032	0.00037 ± 0.00003	2.37 ± 0.21	MSWD = 2.2	0.00038 ± 0.00006	2.46 ± 0.41	MSWD = 2.1
3.1	53	22	0.020	24.17	2309.6 ± 149.0	0.057 ± 0.0082	0.00033 ± 0.00003	2.12 ± 0.22		0.00034 ± 0.00007	2.21 ± 0.44	
4.1	42	27	0.013	12.21	2753.8 ± 229.7	0.0543 ± 0.0078	0.00032 ± 0.00004	2.05 ± 0.25		0.00033 ± 0.00008	2.14 ± 0.51	
5.1	90	54	0.030	11.90	2604.4 ± 139.4	0.0638 ± 0.0097	0.00034 ± 0.00002	2.18 ± 0.15		0.00035 ± 0.00005	2.27 ± 0.29	
6.1	49	30	0.018	19.43	2322.4 ± 182.9	0.0547 ± 0.0047	0.00035 ± 0.00003	2.24 ± 0.21		0.00036 ± 0.00007	2.32 ± 0.43	
7.1	49	30	0.017	17.48	2488.1 ± 168.2	0.0487 ± 0.0039	0.00033 ± 0.00003	2.14 ± 0.20		0.00035 ± 0.00006	2.22 ± 0.40	
8.1	57	41	0.023	16.64	2131.2 ± 182.9	0.0431 ± 0.0044	0.00039 ± 0.00003	2.52 ± 0.21		0.00040 ± 0.00006	2.60 ± 0.41	
9.1	80	28	0.030	28.86	2302.0 ± 123.6	0.0481 ± 0.0045	0.00031 ± 0.00003	1.99 ± 0.20		0.00032 ± 0.00006	2.09 ± 0.40	
10.1	218	113	0.058	10.60	3212.5 ± 120.3	0.0514 ± 0.0024	0.00028 ± 0.00001	1.79 ± 0.09		0.00029 ± 0.00003	1.88 ± 0.17	
11.1	37	22	0.012	28.88	2718.7 ± 218.6	0.0547 ± 0.0043	0.00026 ± 0.00004	1.69 ± 0.24		0.00028 ± 0.00007	1.77 ± 0.47	



Table 1. (continued)

Grain Sample	Concentrations			Atomic Ratios ^a		207Pb Corrected Ages (Ma)		207Pb and 230Th Corrected Ages		
	U (ppm)	Th (ppm)	206Pb (ppm)	f206 (%)	238U/206Pb ^d (abs err)	207Pb/206Pb ^d (abs err)	206Pb/238U ^e (abs err)	206Pb/238U ^e (abs err)	206Pb/238U ^f (2σ)	Weighted Average Age
<i>ODP Hole 1275D: 75D-167, Plagiogranite Dike in Gabbro</i>										
1.1	321	355	0.128	18.22	2151.0 ± 93.6	0.1899 ± 0.0589	0.00038 ± 0.00004	0.00039 ± 0.00008	2.52 ± 0.50	2.40 ± 0.11
2.1	262	242	0.091	19.65	2481.6 ± 136.9	0.2013 ± 0.0295	0.00032 ± 0.00002	0.00034 ± 0.00005	2.16 ± 0.30	MSWD = 1.06
3.1	265	136	0.097	12.60	2360.7 ± 115.2	0.1456 ± 0.0185	0.00037 ± 0.00002	0.00038 ± 0.00004	2.48 ± 0.27	
4.1	210	185	0.072	10.12	2506.9 ± 132.4	0.1260 ± 0.0190	0.00036 ± 0.00002	0.00037 ± 0.00004	2.39 ± 0.27	
5.1	483	643	0.166	4.27	2508.7 ± 97.3	0.0798 ± 0.0098	0.00038 ± 0.00002	0.00039 ± 0.00003	2.52 ± 0.20	
6.1	104	84	0.054	38.94	1661.11 ± 102.3	0.3536 ± 0.0870	0.00037 ± 0.00007	0.00038 ± 0.00014	2.45 ± 0.91	
7.1	301	284	0.093	4.08	2781.6 ± 134.3	0.0783 ± 0.0119	0.00034 ± 0.00002	0.00036 ± 0.00004	2.30 ± 0.23	
<i>ODP Hole 1275D: 75D-180, Plagiogranite Dike in Gabbro</i>										
1.1	82	49	0.021	8.26	3318.0 ± 205.3	0.0560 ± 0.0061	0.00028 ± 0.00002	0.00029 ± 0.00004	1.87 ± 0.28	2.19 ± 0.09
2.1	81	51	0.025	17.65	2724.9 ± 142.6	0.0684 ± 0.0065	0.00030 ± 0.00002	0.00032 ± 0.00004	2.03 ± 0.29	MSWD = 1.7
3.1	102	73	0.029	5.38	3026.4 ± 153.3	0.0832 ± 0.0154	0.00031 ± 0.00002	0.00033 ± 0.00004	2.10 ± 0.26	
4.1	55	33	0.020	12.63	2382.1 ± 149.3	0.0658 ± 0.0065	0.00037 ± 0.00003	0.00038 ± 0.00006	2.45 ± 0.37	
5.1	270	197	0.090	15.08	2591.1 ± 77.5	0.0711 ± 0.0089	0.00033 ± 0.00001	0.00034 ± 0.00003	2.19 ± 0.19	
6.1	280	151	0.081	0.30	2970.9 ± 93.5	0.0513 ± 0.0062	0.00034 ± 0.00001	0.00035 ± 0.00002	2.25 ± 0.15	
7.1	385	217	0.107	2.71	3101.3 ± 86.7	0.0428 ± 0.0068	0.00031 ± 0.00001	0.00033 ± 0.00002	2.11 ± 0.13	
8.1	408	228	0.127	6.24	2767.5 ± 69.0	0.0580 ± 0.0058	0.00034 ± 0.00001	0.00035 ± 0.00002	2.27 ± 0.13	
9.1	120	94	0.040	10.90	2595.1 ± 114.4	0.0627 ± 0.0117	0.00034 ± 0.00002	0.00036 ± 0.00004	2.29 ± 0.25	
<i>ODP Hole 1275D: 75D-200, Plagiogranite Dike in Noritic Gabbro</i>										
1.1	28	16	0.007	9.87	3318.0 ± 412.0	0.125 ± 0.060	0.00027 ± 0.00004	0.00029 ± 0.00008	1.84 ± 0.53	2.26 ± 0.15
2.1	72	55	0.024	10.62	2568.4 ± 148.6	0.131 ± 0.027	0.00035 ± 0.00002	0.00036 ± 0.00005	2.32 ± 0.32	MSWD = 1.8
3.1	44	16	0.016	27.83	2376.9 ± 166.2	0.268 ± 0.050	0.00030 ± 0.00004	0.00032 ± 0.00007	2.05 ± 0.48	
4.1	47	27	0.015	22.98	2711.9 ± 200.6	0.230 ± 0.048	0.00028 ± 0.00003	0.00030 ± 0.00006	1.92 ± 0.42	
5.1	201	159	0.064	4.13	2683.7 ± 99.0	0.079 ± 0.016	0.00036 ± 0.00002	0.00037 ± 0.00003	2.38 ± 0.20	
6.1	57	32	0.021	12.63	2369.0 ± 146.2	0.147 ± 0.031	0.00037 ± 0.00003	0.00038 ± 0.00006	2.47 ± 0.37	
7.1	45	26	0.015	6.38	2654.3 ± 203.3	0.097 ± 0.043	0.00035 ± 0.00004	0.00037 ± 0.00007	2.36 ± 0.44	
8.1	31	14	0.012	7.07	2232.2 ± 176.6	0.103 ± 0.024	0.00042 ± 0.00004	0.00043 ± 0.00007	2.78 ± 0.46	
9.1	97	49	0.031	18.41	2661.5 ± 132.9	0.193 ± 0.029	0.00031 ± 0.00002	0.00032 ± 0.00004	2.07 ± 0.29	
10.1	62	36	0.020	7.96	2588.7 ± 170.6	0.110 ± 0.024	0.00036 ± 0.00003	0.00037 ± 0.00005	2.38 ± 0.34	
11.1	49	28	0.016	25.59	2668.7 ± 189.0	0.251 ± 0.045	0.00028 ± 0.00003	0.00029 ± 0.00006	1.89 ± 0.41	
12.1	51	34	0.016	13.42	2676.2 ± 184.4	0.153 ± 0.033	0.00032 ± 0.00003	0.00034 ± 0.00006	2.17 ± 0.36	
<i>ODP Hole 1270D: 70D-19, Altered Gabbroic Vein in Peridotite</i>										
1.1	35	27	0.006	35.50	4748.8 ± 536.9	0.330 ± 0.088	0.00014 ± 0.00003	0.000148 ± 0.000056	0.96 ± 0.36	1.28 ± 0.03
1.2	39	30	0.008	22.74	4127.9 ± 452.9	0.228 ± 0.067	0.00019 ± 0.00003	0.000200 ± 0.000058	1.29 ± 0.37	MSWD = 1.07
1.3	39	30	0.009	39.05	3959.9 ± 444.4	0.358 ± 0.120	0.00015 ± 0.00004	0.000167 ± 0.000084	1.07 ± 0.54	
1.4	365	194	0.060	6.63	5183.6 ± 204.1	0.099 ± 0.016	0.00018 ± 0.00001	0.000194 ± 0.000016	1.25 ± 0.10	
1.5	276	405	0.047	6.54	5019.8 ± 230.3	0.098 ± 0.018	0.00019 ± 0.00001	0.000195 ± 0.000019	1.26 ± 0.13	

Table 1. (continued)

Grain Sample	Concentrations			Atomic Ratios ^a			²⁰⁷ Pb Corrected Ages (Ma)			²⁰⁷ Pb and ²³⁰ Th Corrected Ages		
	U (ppm)	Th (ppm)	²⁰⁶ Pb ^b (ppm)	<i>f</i> ₂₀₆ ^c (%)	²³⁸ U/ ²⁰⁶ Pb ^d (abs err)	²⁰⁷ Pb/ ²⁰⁶ Pb ^d (abs err)	²⁰⁷ Pb Corrected ²⁰⁶ Pb/ ²³⁸ U ^e (abs err)	²⁰⁶ Pb/ ²³⁸ U ^f (1σ)	Weighted Average Age	²⁰⁶ Pb/ ²³⁸ U ^e (abs err)	²⁰⁶ Pb/ ²³⁸ U ^f (2σ)	Weighted Average Age
1.6	2398	2925	0.421	4.39	4895.5 ± 101.6	0.081 ± 0.006	0.00020 ± 0.00000	1.26 ± 0.03		0.000205 ± 0.000009	1.32 ± 0.06	
1.7	40	29	0.007	35.00	4769.5 ± 539.1	0.326 ± 0.088	0.00014 ± 0.00003	0.88 ± 0.18		0.000149 ± 0.000056	0.96 ± 0.36	
1.8	643	444	0.159	39.95	3463.5 ± 123.0	0.365 ± 0.035	0.00017 ± 0.00002	1.12 ± 0.10		0.000186 ± 0.000031	1.20 ± 0.20	
1.9	1778	614	0.284	3.88	5375.6 ± 94.8	0.077 ± 0.011	0.00018 ± 0.00000	1.15 ± 0.03		0.000194 ± 0.000008	1.25 ± 0.05	
1.10	36	19	0.007	37.13	4155.0 ± 448.0	0.343 ± 0.090	0.00015 ± 0.00003	0.98 ± 0.21		0.000165 ± 0.000065	1.07 ± 0.42	
<i>ODP Hole 1270D: 70D-25, Altered Gabbroic Vein in Peridotite</i>												
1.1	38	28	0.006	37.01	5650.5 ± 766.0	0.342 ± 0.121	0.00011 ± 0.00003	0.72 ± 0.20	1.08 ± 0.04	0.000124 ± 0.000062	0.80 ± 0.40	1.14 ± 0.04
1.2	125	117	0.022	21.88	4823.0 ± 312.3	0.221 ± 0.039	0.00016 ± 0.00001	1.04 ± 0.10	MSWD = 0.64	0.000174 ± 0.000030	1.12 ± 0.19	MSWD = 0.72
1.3	30	23	0.004	30.27	6491.7 ± 1355.0	0.288 ± 0.145	0.00011 ± 0.00004	0.69 ± 0.23		0.000120 ± 0.000072	0.77 ± 0.46	
1.4	290	507	0.049	9.31	5109.5 ± 229.1	0.120 ± 0.025	0.00018 ± 0.00001	1.14 ± 0.07		0.000185 ± 0.000020	1.19 ± 0.13	
1.5	34	25	0.010	36.50	2816.7 ± 284.7	0.338 ± 0.081	0.00023 ± 0.00004	1.45 ± 0.28		0.000238 ± 0.000086	1.54 ± 0.56	
1.6	33	25	0.006	18.58	5156.7 ± 640.8	0.195 ± 0.065	0.00016 ± 0.00003	1.02 ± 0.16		0.000171 ± 0.000051	1.10 ± 0.33	
1.7	38	28	0.008	34.03	4107.8 ± 447.1	0.318 ± 0.061	0.00016 ± 0.00003	1.04 ± 0.17		0.000173 ± 0.000052	1.12 ± 0.34	
1.8	35	26	0.006	29.18	4966.8 ± 607.4	0.279 ± 0.090	0.00014 ± 0.00003	0.92 ± 0.19		0.000155 ± 0.000058	1.00 ± 0.37	
1.9	236	170	0.038	5.13	5307.4 ± 263.8	0.087 ± 0.019	0.00018 ± 0.00001	1.15 ± 0.06		0.000192 ± 0.000020	1.24 ± 0.13	
1.10	34	24	0.006	9.39	4819.6 ± 603.4	0.121 ± 0.060	0.00019 ± 0.00003	1.21 ± 0.18		0.000201 ± 0.000057	1.30 ± 0.36	
1.11	733	1112	0.109	6.36	5780.6 ± 160.8	0.097 ± 0.011	0.00016 ± 0.00001	1.04 ± 0.03		0.000170 ± 0.000010	1.10 ± 0.07	
1.12	406	622	0.064	6.97	5474.8 ± 212.9	0.102 ± 0.016	0.00017 ± 0.00001	1.10 ± 0.05		0.000178 ± 0.000015	1.15 ± 0.10	

^aErrors reported at 1σ.

^bRadiogenic ²⁰⁶Pb.

^cFraction of ²⁰⁶Pb that is common.

^dUncorrected, measured ratios. Abs err, absolute error.

^eThe ²⁰⁷Pb corrected ratios using age appropriate model Pb isotopic composition of Stacey and Kramers [1975].

^fThe ²⁰⁷Pb corrected age; spot analyses in italics had high (cutoff) was set at >30% common lead (*f*₂₀₆), and were excluded from age determinations.

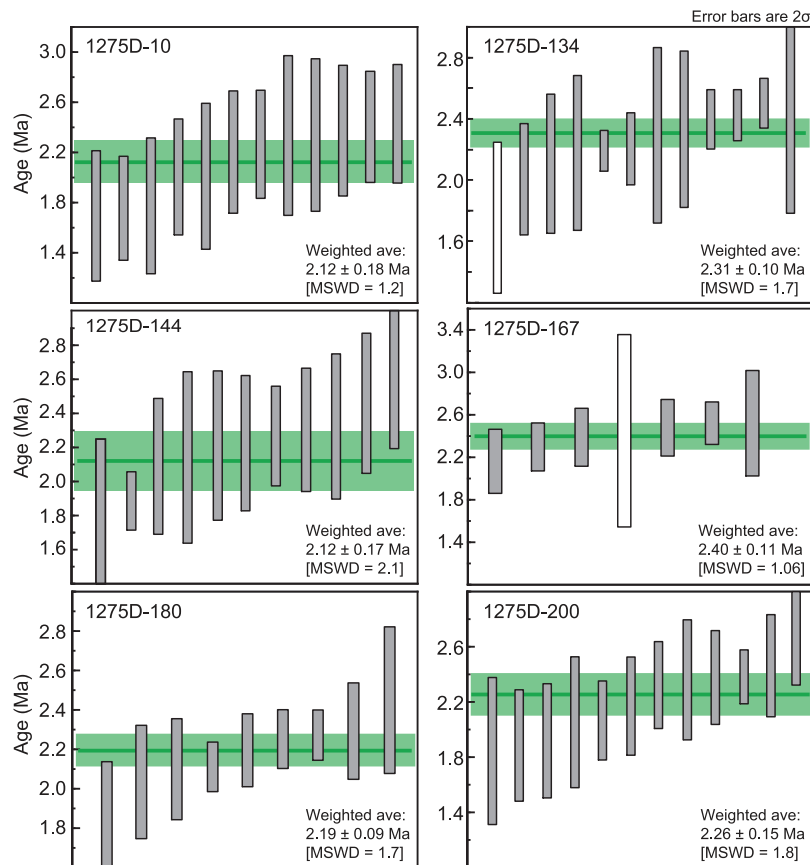


Figure 5. The ^{207}Pb corrected $^{206}\text{Pb}/^{238}\text{U}$ zircon ages for rock samples collected in ODP Hole 1275D ($15^{\circ}44'\text{N}$, MAR). Ages have been corrected for ^{230}Th disequilibrium (see text for details). Spot analyses shown as unfilled bars were rejected when calculating weighted averages on the basis of high initial common lead ($f_{206} > 30\%$). The weighted average age and 95% confidence limit for each rock sample are shown graphically as a dark green line and light green bar, respectively.

rocks collected 144–200 mbsf) give similar ages ranging from 1.57 ± 0.14 to 1.77 ± 0.16 Ma (Table 2), which are not distinguishable given measurement uncertainties. Assuming any scatter is analytical and that these closely spaced samples (<60 m apart) record the same cooling history, we calculate a weighted average (U-Th)/He age of is 1.66 ± 0.09 Ma (2σ) for these three grains. In contrast, sample 1275D-10 yields a corrected (U-Th)/He age that is older than the Pb/U zircon age. A possible cause of the “too old” age is U-Th zonation within the crystal, such as the presence of a highly uranium-rich core and uranium-depleted rim, which results in more complete ^4He retention than expected [e.g., Reiners, 2005]. In this case, the alpha ejection correction applied would not be appropriate (we note that the uncorrected age would be geologically reasonable). Grain imaging was not carried out prior to ^4He analysis or subsequent dissolution for ICP-MS analysis. Thus, further evaluation is not

possible, and the (U-Th)/He age of sample 1275D-10 is discarded from the following discussion. Uranium-enriched cores are rare in ocean crust zircons examined previously [e.g., Schwartz *et al.*, 2005; Grimes *et al.*, 2009], and the (U-Th)/He cooling age of the three samples from 144 to 200 mbsf in core 1275D is notably reproducible. Therefore, the simplest explanation is that these three samples reflect synchronous cooling to below 200°C , such as would occur during uplift of this crustal block along a fault. Considering the weighted average Pb/U sample ages and the single-grain (U-Th)/He ages, the time-averaged cooling rates for these three rocks range from 886°C to $1453^{\circ}\text{C}/\text{Myr}$ (Table 3) over the temperature interval $\sim 820^{\circ}\text{C}$ – 210°C . The average cooling rate (calculated by combining the Pb/U and (U-Th)/He zircon ages for the three samples from 144 to 200 mbsf in core 1275D) is $1162(^{+838}_{-343})^{\circ}\text{C}/\text{Myr}$. The uncertainties quoted for cooling rates were calculated from the

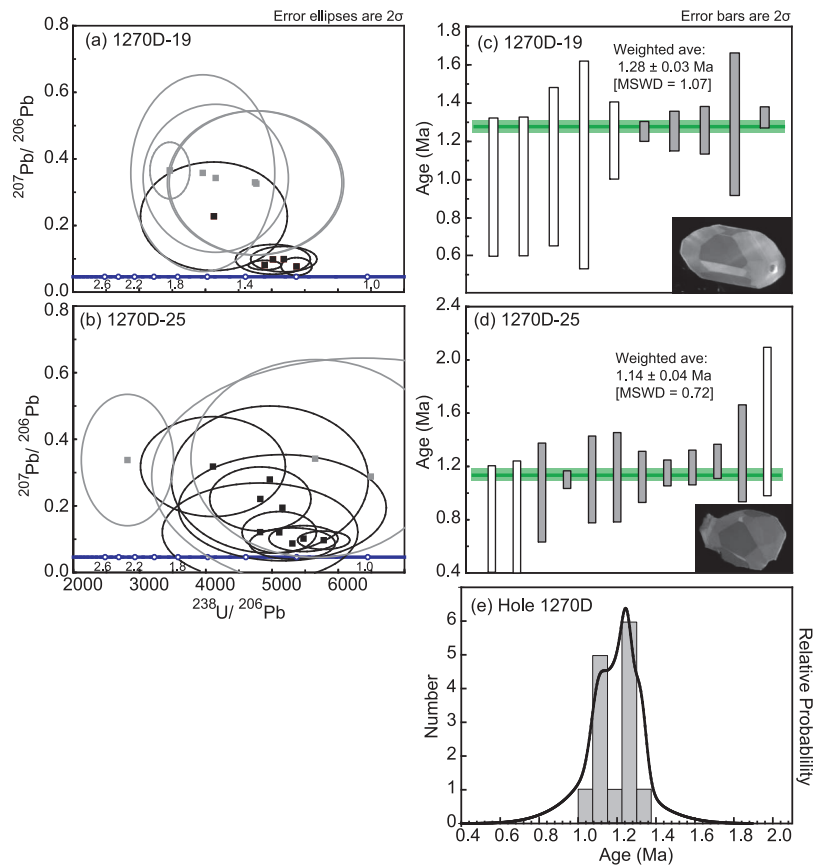


Figure 6. Zircon ages from core 1270D. (a–b) *Tera and Wasserburg* [1972] concordia plots. (c–d) ^{207}Pb – ^{230}Th corrected $^{206}\text{Pb}/^{238}\text{U}$ zircon ages. Errors on spot analyses are 2σ . Spot analyses shown as unfilled bars (and gray ellipses in Figures 6a and 6b) were rejected on the basis of high initial common lead ($f_{206} > 30\%$). Including all the spot analyses in the weighted average age calculation for each rock sample increases the MSWD significantly, but changes the calculated ages and errors by less than 0.01 Ma. The weighted average age and 95% confidence limit for each rock sample are shown graphically as a dark green line and light green bar, respectively. (e) Histogram and probability density function for the combined accepted spots used from 1270D-19 and 1270D-25.

Table 2. (U-Th)/He Isotopic Analysis of Ocean Crustal Zircons

Sample Name	U (ppm)	Th (ppm)	Th/U	^4He (ncc)	Mass (μg)	MWAR ^a (μm)	F_T ^b	Uncorrected (U-Th)/He Age (Ma)	Corrected (U-Th)/He Age ^c (Ma)
70D25zA	37.1	28.0	0.75	0.0529	14.80	53	0.818	0.68	0.83 ± 0.07
75D105zA	25.8	12.7	0.49	0.0558	7.72	46	0.788	2.08	2.64 ± 0.24^d
75D144zA	129.1	70.2	0.54	0.1600	6.95	50	0.792	1.31	1.65 ± 0.15
75D180zA	208.0	117.1	0.56	0.3021	7.57	52	0.792	1.40	1.77 ± 0.16
75D200zA	92.3	42.8	0.46	0.3941	23.63	74	0.858	1.35	1.57 ± 0.14
3646-1205zA	19.5	10.1	0.52	0.0154	11.45	63	0.826	0.51	0.62 ± 0.06
3646-1205zB	16.7	9.5	0.57	0.0251	19.26	59	0.835	0.57	0.68 ± 0.06

^aMWAR, mean weighted average radius.

^b F_T , fraction of He retained.

^cAges corrected for alpha ejection following methods of *Farley et al.* [1996] and *Reiners* [2005]. Errors are presented at 2σ level and include analytical errors and uncertainties from reproducibility of the Fish Canyon Tuff standard [*Reiners*, 2005]. The 1275D weighted average is 1.66 ± 0.09 (2σ , internal error); 3646-1205 weighted average is 0.65 ± 0.04 (2σ , internal error).

^dDiscarded; older than Pb/U age.

Table 3. Constraints From Thermochronometry on Active Fault Lengths and Thermal Structure Assuming a Fault Initiation Dip of 50°

Location (Sample)	Temperature Interval (°C)	Time Interval (Ma)		Cooling Rates			Spreading Rate (km/Myr)	Length of Fault System ^a (km)		Depth to ~850°C ^b (kmsf)		Mean Thermal Gradient (°C/km)	Time-Temperature Constraints	Source ^c
		Mean	± (2σ)	Ave.	Min	Max		Mean	±	Mean	±			
Fifteen-Twenty Fracture Zone														
Core 1275D ave. ^d	820–210	0.53	0.22	1162	819	2000	16	8.4	4.2	6.9	3.0	88	Pb/U and (U-Th)/He	this study
Core 1275D ave. (1275D–144)		0.53	0.22	1162	819	2000	13	6.8	2.9	6.2	2.0	98	Pb/U and (U-Th)/He	
(1275D–180)		0.47	0.32	1307	777	4123								
(1275D–200)		0.42	0.25	1453	912	3576								
1270D–25 ^d	830–210	0.69	0.29	886	622	1535	16	5.0	2.1	4.8	1.4	129	Pb/U and (U-Th)/He	this study
1270D–25		0.31	0.11	1997	1475	3094	13	4.0	1.4	4.1	0.9	152	Pb/U and (U-Th)/He	
Atlantis Massif, MAR														
<i>Alvin</i> 3646–1205	850–210	0.42	0.07	1524	1306	1829	20	8.4	1.4	6.9	0.9	92	Pb/U and (U-Th)/He	1, this study
Atlantis Bank, SWIR														
ODP Hole 735B	820–365	0.55	0.27	827	555	1625	14	7.7	3.8	6.9	2.7	47	Pb/U and Ar/Ar biotite	2, 3
Surface samples	820–210	0.41	0.98	1488	439	–	14	5.7	13.7	3.9	10.3	32	Pb/U and (U-Th)/He	3, 4

^aLength is calculated from the time interval over which samples were translated along a fault system during cooling from ~850°C to ~200°C and the estimated spreading rate. Uncertainties are estimated by considering the extremal limits on the time interval allowed by the age errors.

^bCalculated from the length of the fault assuming a continuous, curved fault initiating at a dip of 50°, plus an estimated depth to the 200°C isotherm of 1.5 km.

^cReferences: 1, *Grimes et al.* [2008]; 2, *Jolin et al.* [2004]; 3, *Baines et al.* [2009]; 4, *Schwartz et al.* [2009].

^dSpreading rate assuming 65% asymmetric accretion during active faulting. Ave., average.

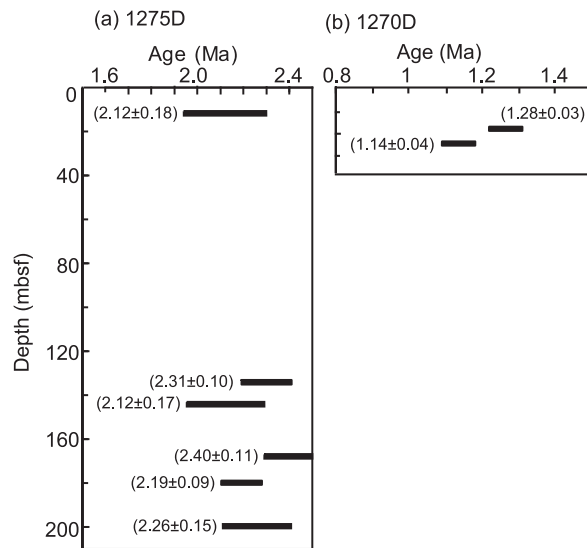


Figure 7. Depth versus Pb/U age in ODP cores (a) 1275D and (b) 1270D. The weighted mean age and 95% confidence limit (in Ma) for each sample is given in parentheses. Resolvable age differences occur in both holes and imply episodic magma intrusion.

extremal limits defined by 95% confidence uncertainties on the Pb/U and (U-Th)/He ages.

3.3.3. Results From Core 1270D

[28] The single grain analyzed from sample 1270D-25 gave a (U-Th)/He age of 0.83 ± 0.07 Ma, indicating the rock cooled to $\sim 200^\circ\text{C}$ in 0.3 Myr following zircon crystallization. The time-averaged cooling rate determined from the Pb/U and (U-Th)/He zircon ages is $1997^{(+1097}_{-522)}^\circ\text{C/Myr}$ (Table 3).

3.3.4. Results From Atlantis Massif

[29] Two zircon grains from sample 3646-1205 were analyzed. The replicate ages are indistinguishable, and together yield a weighted average (U-Th)/He age of 0.65 ± 0.04 Ma (2σ internal error). Taken with the Pb/U zircon age of 1.07 ± 0.03 reported by Grimes *et al.* [2008], this sample records a time-averaged cooling rate of $1524^{(+305}_{-218)}^\circ\text{C/Myr}$ from 850°C to 210°C (Table 3).

4. Discussion and Implications

[30] The isotopic ages presented here provide new constraints on the timing and duration of magma emplacement, and thermal evolution of deep seated oceanic lithosphere that has been denuded to the seafloor by detachment faulting. Integrating Pb/U

and (U-Th)/He zircon with constraints from magnetic anomaly ages enables us to construct comprehensive T-t paths and quantify the time averaged cooling history over the temperature interval $\sim 850^\circ\text{C}$ – 200°C .

4.1. Magmatic Crustal Accretion

[31] The Pb/U zircon ages provide a minimum age of emplacement for magmas building lower oceanic crust. Cooling rates determined for very high temperatures ($>600^\circ\text{C}$) using Ca-in-olivine diffusion indicate extremely rapid cooling in samples of lower oceanic crust from the Oman ophiolite, Hess Deep (EPR), ODP Hole 735B (SWIR), and ODP Hole 923A (MAR) (10^3°C – 10^5°C/Myr) [Coogan *et al.*, 2007; VanTongeren *et al.*, 2008]. The range of closure temperatures reported for Ca-in-olivine diffusion is $>600^\circ\text{C}$ – 1000°C [Coogan *et al.*, 2007], though cooling rates determined using this method typically reflect higher temperatures $>800^\circ\text{C}$ [e.g., VanTongeren *et al.*, 2008]. Considering these rapid high-temperature cooling rates and the estimated zircon crystallization temperatures, Pb/U zircon ages for the felsic differentiates would underestimate the intrusion age of magma emplaced at $\sim 1000^\circ\text{C}$ by 20–200 kyr.

[32] Crystallization ages from samples collected near the 15°20' Fracture Zone provide an estimate for the duration over which magma was supplied during construction of two relatively short crustal sections. The ages from samples at 167 (2.40 ± 0.11 Ma) and 180 mbsf (2.19 ± 0.09 Ma) in core 1275D indicate a duration of at least 40 kyr for magma emplacement. This duration represents a minimum estimate for the emplacement of the entire gabbroic section sampled by core 1275D, since only late-stage felsic rocks hosting zircon can be dated. Zircon ages from 5 of the 6 samples collected in core 1275D between 10 and 200 mbsf yield ages within error of one another (Figure 7), implying that the majority of the crustal section formed within the resolution of the dating method. In core 1270D, the 2 altered dikes collected less than 6 m apart also yield different ages (Figure 6). The difference in the age of these two samples could reflect magma intrusion spanning >70 kyr, similar to the duration implied from the ages in core 1275D. However, poor recovery from Hole 1270D, and the recovery of fault rocks between 15 and 20 mbsf in all 4 holes drilled at Site 1270 [Kelemen *et al.*, 2004; Schroeder *et al.*, 2007] precludes unambiguous interpretation of this age difference. Relative displacement of these two samples

during faulting is also possible. Assuming a slip rate equivalent to the half-spreading rate of 13 mm/yr and an initially uniform vertical age profile, sample 1270D-19 would have had to have been translated ~2 km toward the ridge axis relative to 1270D-25 to account for the difference in the average ages (140 kyr). Unfortunately, we are unable to resolve the magnitude of fault slip to further evaluate the likelihood of this possibility.

[33] The period of accretion implied by zircon ages from ODP holes 1275D and 1270D is similar to durations found at other multiply intruded gabbroic sections sampled from oceanic core complexes. In IODP Hole U1309D at 30°N, MAR, sample ages distributed throughout a 1.4 km vertical borehole document accretion spanning ~200 kyr [Grimes *et al.*, 2008]. At Atlantis Bank (ODP Hole 735B), Pb/U zircon ages indicate that this 1.5 km crustal section could have grown over similar timescales [Baines *et al.*, 2009]. Using the high precision TIMS dating technique, Lissenberg *et al.* [2009] was able to identify similar age ranges (90–235 kyr) within single rocks collected from the Vema Fracture Zone, MAR. Further, the geochronologic results are consistent with a multicomponent magnetic remanence study of multiply intruded gabbros from the Kane Fracture Zone, MAR, which concluded that the emplacement of adjacent intrusions was separated by >210 kyr [Meurer and Gee, 2002; Gee and Meurer, 2002]. We therefore infer that typical timescales for magmatic crustal growth during formation of the gabbroic crust over length scales of 100 m–1.5 km are ~100–300 kyr. Along the MAR, this duration reflects several kilometers of spreading away from an initial zone of magma intrusion.

4.2. Cooling of Lower Crust Exposed in the Footwalls to Large Displacement Normal Faults

4.2.1. Cooling Along the MAR

[34] The time-integrated cooling rates along the MAR for the three areas investigated here range from ~1000°C–2000°C/Myr over the temperature interval ~850°C–210°C. These are consistent with cooling rates for “rapidly cooled” samples from Atlantis Bank (>1200°C/Myr) [Schwartz *et al.*, 2009] determined using these same techniques. The rates are similar to the slowest cooling rates measured using Ca-in-olivine diffusion in slow-spreading crust (~1250°C–10,000°C/Myr) [Coogan *et al.*, 2007].

[35] Thermochronometric data are shown in Figure 8 with reference conductive cooling curves determined using a plate-cooling model for the oceanic lithosphere [e.g., Stein and Stein, 1992]. The calculated cooling rates are faster in core 1270D (~2000°C/Myr) than for other locations, although it must be noted that the difference is near the limits of the resolution of the data. However, more rapid cooling might be expected to arise from the smaller thermal mass associated with the thin dikes in 1270D, or possibly shallower emplacement within the lithosphere.

[36] The cooling histories of all three locations are shown together on Figure 9, along with thermo-chronometric results at Atlantis Bank [John *et al.*, 2004; Schwartz *et al.*, 2009] and the range of rates determined for slow- and ultraslow-spreading crust by Ca-in-olivine diffusion studies [Coogan *et al.*, 2007]. To facilitate direct comparison of cooling histories recorded by samples with different crystallization ages, all sample ages are plotted relative to the Pb/U age of that sample (with Pb/U age of each sample plotted at 0). The present-day bottomhole temperature in IODP Hole U1309D (1415 mbsf), estimated ~140°C based on logging results shortly after the hole was drilled [Blackman *et al.*, 2006], is also shown in Figure 9. A Pb/U zircon age of 1.20 ± 0.03 Ma was measured on a sample from the bottom of core U1309D [Grimes *et al.*, 2008]. A conductive cooling curve for 1500 mbsf is shown for reference, together with cooling curves derived from the crustal extension models of Tucholke *et al.* [2008] as discussed below.

4.2.2. Cooling During Faulting

[37] While conductive cooling curves (Figure 8) provide a framework for comparing cooling profiles defined by the thermo-chronometric data, they do not account for hydrothermal circulation or the fact that these samples were denuded from some depth beneath the rift valley along faults, and exposed on the seafloor. To examine the effect of faulting and denudation on cooling, we have extracted cooling profiles from the existing numerical models of Tucholke *et al.* [2008] initially developed to investigate the role of magmatism during formation of long-lived, large-offset normal faults. The models were generated assuming symmetric spreading at a full rate of 50 mm/yr, and an initially uniform temperature structure that evolves in time with accompanying magma injection, mantle flow, and faulting. The models account for hydrothermal

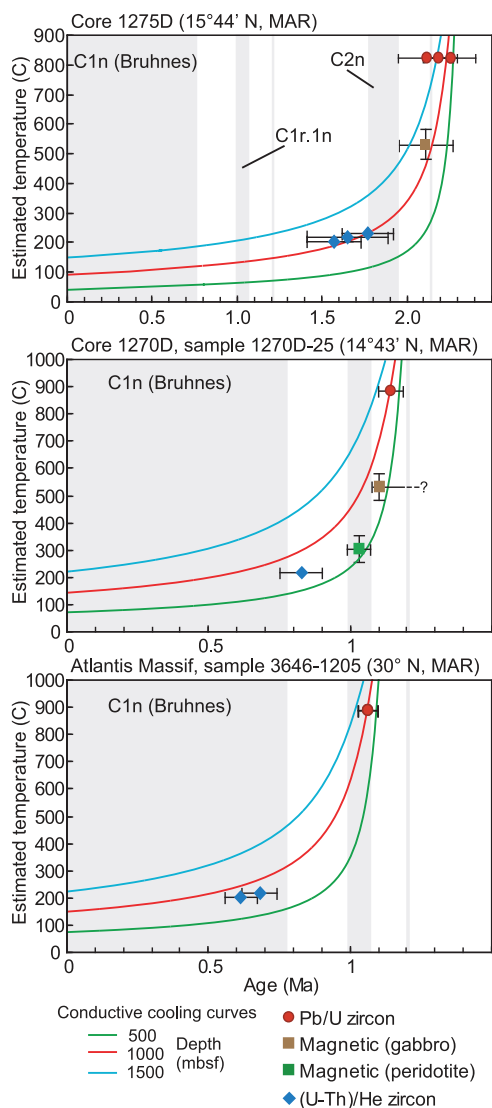


Figure 8. Temperature-time plots showing thermo-chronometric data along with reference conductive cooling curves calculated for a plate-cooling model [Stein and Stein, 1992]. Model curves assume an initial temperature of 1300°C. A 40 km long ridge-parallel section of the upper 20 km of oceanic lithosphere was modeled, assuming a constant temperature (0°C) upper boundary condition. A 6 km thick crust was included, assuming a density of 2900 kg/m³, specific heat capacity 1000 J/kg/K, and thermal conductivity 2.2 W/m/K, above the mantle with a density of 3300 kg/m³, specific heat capacity 1260 J/kg/K, and thermal conductivity of 3.15 W/m/K. The conductive cooling curves are positioned beginning at an age 50 kyr older than the mean Pb/U zircon age in each location. Shaded gray fields indicate normal polarity magnetic intervals based on the magnetic timescale of Ogg and Smith [2004].

circulation by increasing the thermal conductivity by a factor (Nusselt number, Nu) for the upper 7 km [Tucholke *et al.*, 2008]. The models use $Nu = 8$ to achieve a brittle layer thickness of 5 km, consistent with the average maximum depth of seismicity along the MAR [Kong *et al.*, 1992; Wolfe *et al.*, 1995; Barclay *et al.*, 2001].

[38] We interpolated the 900°C, 600°C, and 200°C isotherms from their model accommodating 50% extension by magma emplacement ($M = 0.5$) (Figure 10), since this model was shown to support the generation of long-lived faults [Tucholke *et al.*, 2008]. The isotherms were extracted near the end of the model run (at ~1.3 Myr) when a steady state thermal structure had been achieved. Cooling profiles were determined both for a rock denuded adjacent to the detachment fault, and at 1.4 km below the fault by measuring the distance between the isotherms (Figure 10). This distance is inverted to time assuming the spreading rate used in the modeling (half rate = 25 mm/yr), as well as a slower half spreading rate of 15 mm/yr, comparable to symmetric half rate of the current study areas. These curves are shown on Figure 9 with the thermochronometric data presented here and for Atlantis Bank [John *et al.*, 2004; Schwartz *et al.*, 2009].

[39] The cooling profiles extracted from the models by Tucholke *et al.* [2008] reflect possible cooling paths for a rock body emplaced at ~5–6 km depth and denuded to the seafloor along a curved detachment fault. The cooling curve determined assuming a half-spreading rate of 15 mm/yr closely approximates data from the most rapidly cooled sample from core 1270D; samples from other locations record slower cooling (Figure 9). Differences between the extracted cooling profiles and the thermochronometric data may arise because of necessary simplifications associated with the models, and the fact that these models were generated for a full spreading rate twice that of any of the study locations. In particular the models simplify the complexities of magma intrusion at the axis and hydrothermal circulation through the footwall and along the fault zones. Protracted or episodic hydrothermal circulation along the fault zone could buffer the temperature along the fault, and modify cooling rates depending on the temperature of the circulating fluids [e.g., McCaig *et al.*, 2010]. At slower spreading rates, the magma (heat) flux at the ridge axis might be less and cooling could depress isotherms to deeper crustal levels, resulting in a thicker thermal boundary layer, a more shallow geothermal gradient, and therefore slower cooling

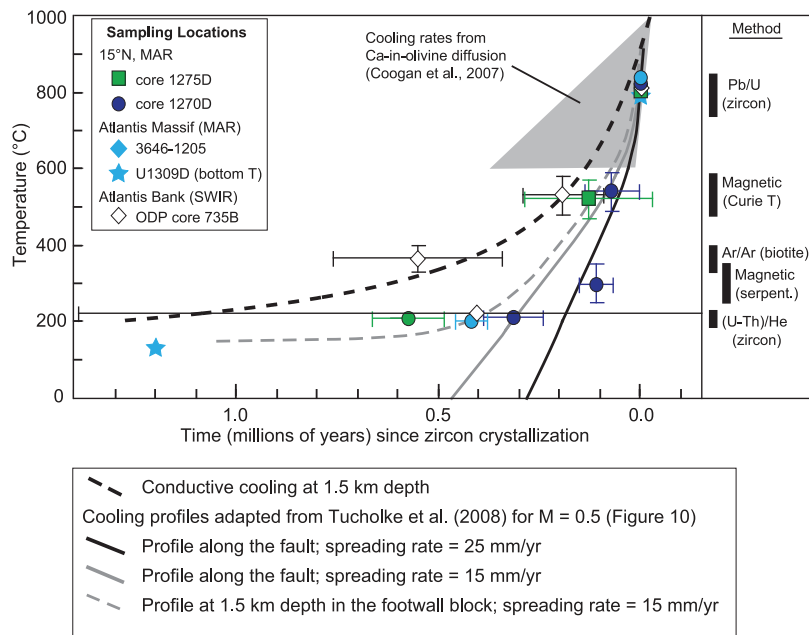


Figure 9. Summary of existing thermochronometric constraints on the cooling of lower oceanic crust (from the MAR and SWIR) that has been denuded to the seafloor during large-offset normal faulting. The ages determined for each sample have been normalized to the respective Pb/U (zircon) age (Pb/U age for all samples plots at 0) to facilitate direct comparison of cooling histories for different locations. Conductive cooling at 1.5 km depth shown as a black dashed line. Solid curves and the dashed gray curve were extracted from Figure 10, after the models of *Tucholke et al.* [2008] for $M = 5$. The solid black curve assumes a spreading rate that is the same as the model (25 mm/yr half rate); the gray curves (solid and dashed) assume a slower half rate = 15 mm/yr. The solid lines are cooling profiles just below the detachment fault in Figure 10; dashed gray curve depicts cooling at 1.5 km depth below the detachment fault, and is shown for comparison with the bottomhole temperature measured in IODP Hole U1309D (shown as star) following drilling [Blackman et al., 2006]. The column at far right depicts the dating method and inferred range of corresponding closure temperature.

rate [e.g., *Sleep, 1975; Shen and Forsyth, 1995; Kelemen et al., 2007*]. The cooling profile presented here for a 15 mm/yr half-spreading rate should therefore be considered an upper bound for the cooling rates of crust spreading at a half rate of 15 km/Myr under conditions similar to those used in the models [*Tucholke et al., 2008*].

4.3. Using Thermal Histories to Evaluate Fault Geometry

[40] The chronometers used here to date rocks from the shallow footwall of large-slip normal fault systems record the time interval between zircon crystallization at $\sim 850^\circ\text{C}$ and cooling through the

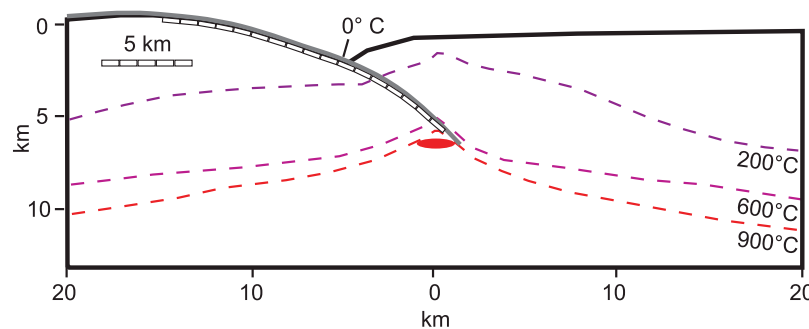


Figure 10. Model thermal structure during detachment faulting after *Tucholke et al.* [2008]. Detachment fault follows the model geometry for $M = 5$; the fault is shown as a thick gray line, with increments marked at 1 km intervals. The approximate locations of the 900°C , 600°C , and 200°C isotherms are indicated. Cooling profiles in Figure 9 were developed by measuring the distance between isotherms and inverting distance to time based on spreading rates of 25 mm/yr and 15 mm/yr.

closure temperature of the (U/Th)-He system at $\sim 200^\circ\text{C}$, which would have been coincident with denudation to the seafloor. Assuming the footwall rocks were unroofed along a single fault system, and that the position of isotherms is approximately at steady state, the time interval defined by the difference in Pb/U and (U-Th)/He ages for rocks collected in the footwall can be used to estimate the length scale of the detachment fault, if the fault slip rate is known.

4.3.1. Are the Studied Areas Single Faults?

[41] The continuous and smooth seafloor bathymetry where fault rocks have been recovered suggest that these core complexes represent material denuded along a single fault system [e.g., *MacLeod et al.*, 2009]. Additionally, the roughly planar distribution of earthquakes defining an inferred active detachment fault located beneath the TAG hydrothermal field at 26°N , MAR, implies a single, continuous fault system to depths of 3–7 km below seafloor [*deMartin et al.*, 2007]. Moreover, two-pyroxene thermometry of mylonites within ODP Hole 735B (Atlantis Bank core complex) and Atlantis Massif suggest that strain was initially localized at temperatures $>800^\circ\text{C}$ [*Schroeder and John*, 2004; *Mehl and Hirth*, 2008; *Miranda and John*, 2010]. Thus, there is evidence to support the interpretation that footwall rocks were denuded along single fault systems, initiated at high temperatures similar to those recorded by Ti-in-zircon crystallization temperatures.

4.3.2. When Did Hydrothermal Circulation Occur?

[42] *Kelemen et al.* [2004] conclude that the core from ODP Hole 1275D underwent fluid interaction and alteration during progressive cooling and uplift, with alteration linked to the deformation associated with detachment faulting. The consistency of the three (U-Th)/He ages measured for rocks from the lower part of core 1275D, from 144 mbsf to 200 mbsf, is best explained by these samples cooling below 200°C during unroofing associated with detachment faulting, and not related to localized hydrothermal flow in the denuded footwall. Consequently we suggest that the assumption that the (U-Th)/He ages record passage through a relatively steady state 200°C isotherm during exhumation is robust. Samples from core 1270D shows the most rapid cooling of all the samples, and hence is unlikely to have been subjected to reheating during

a late, localized hydrothermal event. The serpentinization reportedly occurring at temperatures of $\sim 350^\circ\text{C}$ to $<250^\circ\text{C}$ [e.g., *Bach et al.*, 2004] would have occurred during progressive cooling, and apparently did not result from a later or prolonged (at the resolution of the age data) hydrothermal event. There are fewer constraints for the sample from Atlantis Massif. However, given that it generates a similar cooling rate to the samples from 1275D, we argue that it also likely records passage through a steady state 200°C isotherm rather than recording a later, localized hydrothermal event.

4.3.3. Estimates of Fault Length

[43] Large-offset detachment faults at mid-ocean ridges commonly serve as the plate boundary [*Allerton et al.*, 2000; *Schroeder and John*, 2004; *Buck et al.*, 2005; *Baines et al.*, 2008], with the fault slip rate corresponding to the plate spreading rate at the time faulting was occurring. Using spreading rates determined from Pb/U zircon ages at Atlantis Bank (14 km/Myr) [*Baines et al.*, 2008] and Atlantis Massif (~ 20 km/Myr) [*Grimes et al.*, 2008], we calculate that the $\sim 850^\circ\text{C}$ and $\sim 200^\circ\text{C}$ isotherms were separated by 7.7–8.4 km along the fault plane (Table 3), assuming that the isotherms are approximately steady state. Although we do not know the actual spreading rate during formation of the corrugated structures at $15^\circ 44'$ and $14^\circ 43'\text{N}$, MAR, we speculate that spreading rates were asymmetric based on observations from other core complexes. For example, during the formation of Atlantis Bank it is estimated from both magnetic anomaly data and Pb/U zircon ages that spreading was highly asymmetric, with up to 80% of the full-spreading rate accommodated by the Antarctic plate [*Baines et al.*, 2008]. Similar asymmetry is reported during formation of Atlantis Massif, (70%–100%) [*Grimes et al.*, 2008], the Kane Fracture Zone core complexes ($>60\%$) [*Williams*, 2007; *Cheadle et al.*, 2008], and Fuji Dome (77%) [*Searle et al.*, 2003]. Assuming a rate of 16 km/Myr ($\sim 65\%$ spreading asymmetry), samples from core 1275D indicate a fault system length of 8.4 km. Similarly, 65% asymmetry for the sample from core 1270D yields a shorter fault length of ~ 5 km, reflecting the shorter time interval of recorded cooling. Although this data set does not provide independent information on the geometry of the fault system, the cooling data does place important constraints on possible length scales over the recorded tempera-

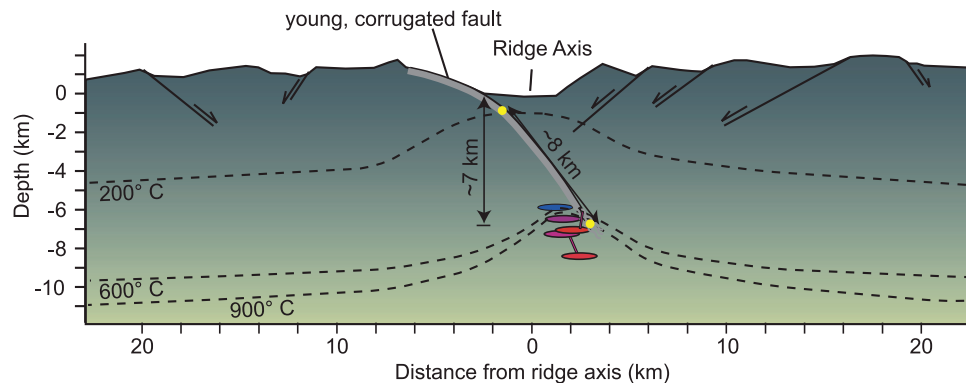


Figure 11. Generalized model of detachment faulting at Atlantis Massif (MAR), Atlantis Bank (SWIR) and the 15°44'N core complex (MAR). Length scale of actual fault systems is based on the local spreading rate and the time interval recorded by cooling from ~850°C (zircon crystallization) to ~200°C ((U-Th)/He zircon age). Intersection of the fault system with these isotherms is indicated as yellow dots. A rolling hinge style fault is shown, initiating with a steep dip and then rolling over to more gentle dips through near constant curvature. See Table 3 for fault system length scales specific to each location studied. In this model, the fault system roots at the base of the lithosphere [e.g., *Tucholke et al.*, 1998] and near the zone of gabbro crystallization in the footwall (red, purple, and blue ellipses).

ture interval, and model detachment fault geometries should be consistent with these results.

4.3.4. Converting Fault Lengths to Fault Depth

[44] If the initial fault geometry were known, the length scales calculated above can be used to estimate the depth of the ~850°C isotherm (i.e., recorded by zircon crystallization). The initiation angle of presently low-angle, large-displacement detachment faults in ocean crust is debated [e.g., *Escartin et al.*, 2003], but several lines of evidence support a ‘rolling-hinge’ style fault that initiates with a moderate to steep dip, and flattens through flexural rotation [e.g., *Buck*, 1988; *Tucholke et al.*, 1998; *Lavier et al.*, 1999; *Buck et al.*, 2005]. Multibeam bathymetric mapping of several active detachment fault systems on the MAR near 13°N [*Smith et al.*, 2006; *MacLeod et al.* 2009], taken with microseismicity studies from 26°N MAR [*deMartin et al.*, 2007] suggest that oceanic detachment faults initiate at steep dips (~60°–70°), and shallow with slip (and attendant rotation) to very gentle dips (<5°). *Hansen* [2007] estimates rotation of >45° for core complexes at the Kane Fracture Zone based on the slope of the ridge inferred to be the breakaway of the detachment fault. In IODP Hole U1309D at Atlantis Massif, magnetic remanence vectors, from fully oriented samples, are shallow relative to the predicted geocentric axial dipole, and have been used to suggest rotations of $46^\circ \pm 6^\circ$ since cooling below 580°C [*Morris et al.*,

2009], implying an initial dip >50°. Substantial footwall rotations of ~60°–80° are interpreted for faults in the 14°N–16°N, MAR region based on similar paleomagnetic evidence [*Garces and Gee*, 2007]. Based in part on these studies, taken with additional observations from bathymetry and drill-core, *Schroeder et al.* [2007] proposed that the large-displacement faults between 14°N and 16°N on the MAR have a downward curving geometry that evolves from initially steep to gentle dips with increasing offset. A conservative initial dip angle of 50° is chosen for following calculations of fault lengths and vertical distance (i.e., depth) between the ~850°C and ~200°C isotherms (Table 3 and Figure 11).

[45] Converting the calculated fault lengths to absolute depth requires not only an assumption about the initial dip, but also an estimated depth below the seafloor to the 200°C isotherm. Estimated depths for the 200°C isotherm beneath the ridge axis are 1–2 km [e.g., *Morgan and Chen*, 1993; *MacLennan et al.*, 2005]. We assume an intermediate depth of ~1.5 km, consistent with the estimated thermal structure beneath the TAG hydrothermal field (26°10'N, MAR) where active detachment faulting and relatively deep magma emplacement are inferred [*deMartin et al.*, 2007; *Canales et al.*, 2007]. Using this depth estimate to 200°C and an initial fault dip of 50°, the depth of the ~800°C–850°C isotherm during active faulting is calculated to be ~7 km at Atlantis Massif, Atlantis Bank, and from core 1275D, and ~4.8 km from core 1270D



(Table 3). Calculated depths would be 1–2 km greater for an initial dip angle of 70°. If a more gentle dip of ~30° is assumed for the fault exposed at Atlantis Bank (based on evidence from magnetic remanance that the rocks have only undergone ~20° of rotation below the Curie temperature), then a shallower depth of ~5 km is estimated.

[46] These estimated depths to ~850°C also represent minimum emplacement depths for the exposed gabbro, and are generally greater than depths to melt lenses inferred along the slow-spreading MAR [e.g., *Magde et al.*, 2000; *Singh et al.*, 2006], despite being similar to the average thickness of oceanic crust (6 km) [e.g., *Chen*, 1992]. These calculated depths are approximately equivalent to the maximum depths of earthquakes recorded along the inferred active detachment fault at 26°N, MAR [*deMartin et al.*, 2007]. Thus, our calculations suggest that these large displacement normal faults cut through the entire seismic crust, and possibly deeper into the lithosphere. This also implies that gabbroic rocks exposed in the footwalls to these faults were originally emplaced deep, possibly near the base of the crust or within the shallow mantle lithosphere [e.g., *Cannat*, 1996]. In the 14°N–16°N region of the MAR, deep magma emplacement and deeply rooting fault systems are consistent with the suggestion that this interval of the MAR is characterized by a thick thermal boundary layer [*Kelemen et al.*, 2007; *Schroeder et al.*, 2007].

[47] The length scale of these fault systems, as well as initial depths prior to footwall denudation inferred from the thermochronometry reported here (Figure 11), are consistent with deep rooting detachment faults that cut through a thick thermal boundary layer, and root near a brittle-ductile transition [*Tucholke et al.*, 1998; *Tucholke and Lin*, 1994]. Continuation of the fault system to the brittle-ductile transition is supported by ductile and semibrittle fabrics recorded in footwall fault rocks drilled at 14°N–16°N [*Kelemen et al.*, 2004; *Schroeder et al.*, 2007], Atlantis Massif [*Schroeder and John*, 2004; *Boschi et al.*, 2006; *Karson et al.*, 2006], and Atlantis Bank [e.g., *Dick et al.*, 2000; *Mehl and Hirth*, 2008; *Miranda and John*, 2010]. In settings with restricted magmatism, the fault may transition into a high-temperature ductile shear zone that extends deeper into the mantle, ultimately widening into a zone of distributed deformation in the asthenosphere [*John and Cheadle*, 2010]. In contrast, in settings with robust magma supply, the fault may simply root into a transient magma chamber with deformation diffusing into

the melt lens and/or mush zone [*John and Cheadle*, 2010].

5. Conclusions

[48] It is recognized that oceanic core complexes result from a fundamentally distinct mode of sea-floor spreading [e.g., *Cheadle and Grimes*, 2010], but little is known about the cooling histories, depths and timescales of magmatic accretion, and the geometries and depths of their associated detachment faults. Here we investigate the magmatic accretion and thermal evolution of the footwalls of several oceanic core complexes along the MAR near the Fifteen Twenty and Atlantis Fracture zones by combining Pb/U and (U-Th)/He zircon ages of late-stage felsic rocks with magnetic anomaly ages. We present a new approach for defining length scales of detachment faults and estimating depths to which faulting and gabbro emplacement occurs. This approach, combined with additional thermal constraints from the Atlantis Massif (MAR) and Atlantis Bank (SWIR) core complexes, generates a coherent picture of the depths of magmatism and faulting in the footwalls to large displacement normal fault systems that define oceanic core complexes.

[49] The footwalls to these large-offset normal faults cooled to ~200°C roughly 0.3–0.5 Myr after zircon crystallization at ~800°C–850°C, indicating time-averaged cooling rates of ~1000°C–2000°C/Myr. Specifically, we calculate cooling rates of 1162(⁺⁸³⁸₋₃₄₃)°C/Myr in ODP core 1275D, 1997(⁺¹⁰⁹⁷₋₅₂₂)°C/Myr in ODP core 1270D, and 1524(⁺³⁰⁵₋₂₁₈)°C/Myr at Atlantis Massif. In general, cooling histories developed using thermochronometers and magnetic anomaly ages for samples collected in the footwall of large displacement normal faults record rapid cooling histories consistent with cooling during denudation along deep rooting (>5 km) fault systems. We find no evidence for off-axis thermal anomalies for the two core complexes at the Fifteen Twenty Fracture Zone and Atlantis Massif like those observed at Atlantis Bank [e.g., *John et al.*, 2004; *Schwartz et al.*, 2009].

[50] Pb/U zircon dating of rocks collected from 4 vertical boreholes in two oceans (this study) [*Baines et al.*, 2009; *Grimes et al.*, 2008], shows that the time interval over which the majority of magmatic accretion occurs on a 100–1500 m length scale is ~100–300 kyr. The observed age variations within the cores are consistent with a multiple sill



mode of crustal accretion [Grimes *et al.*, 2008], with the age duration reflecting several kilometers of spreading away from, or through the zone of intrusion during construction of gabbroic crust.

[51] The time interval for cooling in the footwall to these large-offset normal faults, taken with the denudation rates of each footwall yields estimates of 5–8.4 km for the distance between the 850°C and 210°C isotherms along the fault plane. Assuming a concave upward fault initiated with a dip of 50° beneath the ridge axis, these length scales imply that the footwalls were denuded from depths of up to ~7 km. Depth estimates decrease or increase by 1–2 km for subsurface dips of 30° or 70°, respectively. These results suggest the detachment faults cut through a thick thermal boundary layer and root up to $\sim 7 \pm 2$ km depth, near or within the brittle-ductile transition, consistent with the high-temperature mylonitic rocks recovered from some detachment faults [Hansen, 2007; Mehl and Hirth, 2008; Miranda and John, 2010]. Given that our Pb/U ages are determined for the most evolved, lowest-temperature rocks in each crustal section, we predict that the majority of gabbro emplacement and crystallization begins at depths >7 km beneath oceanic core complexes.

Acknowledgments

[52] This research used samples and data provided by the Ocean Drilling Program (ODP). Technical assistance from Brad Ito with the sensitive high-resolution ion microprobe and Stefan Nicolescu's efforts in obtaining (U-Th)/He ages for these samples are both gratefully acknowledged. Discussions with Jeff Gee, Peter Kelemen, and Bill Meurer were helpful in developing this paper. This work was supported by NSF OCE grant 0550456 to John, 0352054 to Cheadle and John, and grants from the U.S. Science Support Program (award 48297 to John and 48298 to Grimes). Comments from two anonymous reviewers were helpful in improving this paper.

References

- Allerton, S., J. Escartín, and R. Searle (2000), Extremely asymmetric magmatic accretion of oceanic crust at the ends of slow-spreading ridge segments, *Geology*, *28*, 179–182, doi:10.1130/0091-7613(2000)28<179:EAMAOO>2.0.CO;2.
- Bach, W., C. J. Garrido, H. Paulick, J. Harvey, and M. Rosner (2004), Seawater-peridotite interactions: First insights from ODP Leg 209, MAR 15°N, *Geochem. Geophys. Geosyst.*, *5*, Q09F26, doi:10.1029/2004GC000744.
- Baines, A. G., M. J. Cheadle, B. E. John, and J. J. Schwartz (2008), The rate of oceanic detachment faulting at Atlantis Bank, SW Indian Ridge, *Earth Planet. Sci. Lett.*, *273*, 105–114, doi:10.1016/j.epsl.2008.06.013.
- Baines, A. G., M. J. Cheadle, B. E. John, C. B. Grimes, and J. J. Schwartz (2009), SHRIMP Pb/U zircon ages constrain gabbroic crustal accretion at Atlantis Bank on the ultraslow-spreading Southwest Indian Ridge, *Earth Planet. Sci. Lett.*, *287*, 540–550, doi:10.1016/j.epsl.2009.09.002.
- Barclay, A. H., D. R. Toomey, and S. C. Solomon (2001), Microearthquake characteristics and crustal V_p/V_s structure at the Mid-Atlantic Ridge, 35°N, *J. Geophys. Res.*, *106*, 2017–2034, doi:10.1029/2000JB900371.
- Blackman, D. K., et al. (2002), Geology of the Atlantis Massif (Mid-Atlantic Ridge, 30°N): Implications for the evolution of an ultramafic oceanic core complex, *Mar. Geophys. Res.*, *23*, 443–469, doi:10.1023/B:MARI.0000018232.14085.75.
- Blackman, D. K., B. Ildefonse, B. E. John, Y. Ohara, D. J. Miller, C. J. MacLeod, and the Expedition 304/305 Scientists (2006), *Proceedings of the Integrated Ocean Drilling Program*, vol. 304/305, Integrated Ocean Drill. Program, College Station, Tex., doi:10.2204/iodp.proc.304305.2006.
- Boschi, C., G. L. Früh-Green, A. Delacour, J. A. Karson, and D. S. Kelley (2006), Mass transfer and fluid flow during detachment faulting and development of an oceanic core complex, Atlantis Massif (MAR 30°N), *Geochem. Geophys. Geosyst.*, *7*, Q01004, doi:10.1029/2005GC001074.
- Buck, W. R. (1988), Flexural rotation of normal faults, *Tectonics*, *7*, 959–973, doi:10.1029/TC007i005p00959.
- Buck, W. R., L. L. Lavier, and A. N. B. Poliakov (2005), Modes of faulting at mid-ocean ridges, *Nature*, *434*, 719–723, doi:10.1038/nature03358.
- Canales, J. P., R. A. Sohn, and B. J. deMartin (2007), Crustal structure of the trans-Atlantic geotraverse (TAG) segment (Mid-Atlantic Ridge, 26°10'N): Implications for the nature of hydrothermal circulation and detachment faulting at slow spreading ridges, *Geochem. Geophys. Geosyst.*, *8*, Q08004, doi:10.1029/2007GC001629.
- Cann, J. R., D. K. Blackman, D. K. Smith, E. McAllister, B. Janssen, S. Mello, E. Avgerinos, A. R. Pascoe, and J. Escartín (1997), Corrugated slip surfaces formed at ridge-transform intersections on the Mid-Atlantic Ridge, *Nature*, *385*, 329–332, doi:10.1038/385329a0.
- Cannat, M. (1996), How thick is the magmatic crust at slow spreading oceanic ridges?, *J. Geophys. Res.*, *101*, 2847–2857, doi:10.1029/95JB03116.
- Cannat, M., and J. F. Casey (1995), An ultramafic lift at the Mid-Atlantic Ridge: Successive stages of magmatism in serpentinized peridotite from the 15°N region, in *Mantle and Lower Crust Exposed in Oceanic Ridges and in Ophiolites*, edited by R. L. M. Vissers, and A. Nicolas, pp. 5–34, Kluwer Acad., Dordrecht, Netherlands.
- Cannat, M., D. Bideau, and H. Bougault (1992), Serpentinized peridotites and gabbros in the Mid-Atlantic ridge axial valley at 15°37'N and 16°52'N, *Earth Planet. Sci. Lett.*, *109*, 87–106, doi:10.1016/0012-821X(92)90076-8.
- Cannat, M., Y. Lagabrielle, N. de Coutures, H. Bougault, J. F. Casey, L. Dmitriev, and Y. Fouquet (1997), Ultramafic and gabbroic exposures at the Mid-Atlantic Ridge: Geologic mapping in the 15° region, *Tectonophysics*, *279*, 193–213, doi:10.1016/S0040-1951(97)00113-3.
- Cannat, M., D. Sauter, V. Mendel, E. Ruellan, K. Okino, J. Escartín, V. Combier, and M. Baala (2006), Modes of seafloor generation at a melt-poor ultraslow-spreading ridge, *Geology*, *34*, 605–608, doi:10.1130/G22486.1.
- Cheadle, M., and C. Grimes (2010), To fault or not to fault, *Nat. Geosci.*, *3*, 454–456, doi:10.1038/ngeo910.
- Cheadle, M., B. John, M. Lusk, and J. Wooden (2008), Asymmetric spreading, and the construction of oceanic crust at the



- Kane Oceanic Core Complex, *Eos Trans. AGU*, 89(53), Fall Meet. Suppl., Abstract T41D-04.
- Chen, Y. (1992), Ocean crustal thickness versus spreading rate, *Geophys. Res. Lett.*, 19, 753–756, doi:10.1029/92GL00161.
- Cherniak, D. J., and E. B. Watson (2003), Diffusion in zircon, in *Zircon, Rev. Mineral. Geochem.*, vol. 53, edited by J. M. Hanchar, and P. W. O. Hoskin, pp. 113–143, Mineral. Soc. of Am., Washington, D. C.
- Coogan, L. A., R. N. Wilson, K. M. Gillis, and C. J. MacLeod (2001), Near-solidus evolution of oceanic gabbros: Insights from amphibole geochemistry, *Geochim. Cosmochim. Acta*, 65, 4339–4357, doi:10.1016/S0016-7037(01)00714-1.
- Coogan, L. A., G. R. T. Jenkin, and R. N. Wilson (2002), Constraining the cooling rate of the lower oceanic crust: A new approach applied to the Oman Ophiolite, *Earth Planet. Sci. Lett.*, 199, 127–146, doi:10.1016/S0012-821X(02)00554-X.
- Coogan, L. A., G. R. T. Jenkin, and R. N. Wilson (2007), Contrasting cooling rates in the lower oceanic crust at fast- and slow-spreading ridges revealed by geospeedometry, *J. Petrol.*, 48(11), 2211–2231, doi:10.1093/ptology/egm057.
- deMartin, B. J., R. A. Sohn, J. P. Canales, and S. E. Humphris (2007), Kinematics and geometry of active detachment faulting beneath the trans-Atlantic geotraverse (TAG) hydrothermal field on the Mid-Atlantic Ridge, *Geology*, 35, 711–714, doi:10.1130/G23718A.1.
- Dick, H. J. B., J. H. Natland, J. C. Alt, W. Bach, et al. (2000), A long in situ section of lower ocean crust: Results of ODP Leg 176 drilling at the Southwest Indian Ridge, *Earth Planet. Sci. Lett.*, 179, 31–51, doi:10.1016/S0012-821X(00)00102-3.
- Dodson, M. H. (1973), Closure temperature in cooling geochronological and petrological systems, *Contrib. Mineral. Petrol.*, 40, 259–274, doi:10.1007/BF00373790.
- Escartin, J., and M. Cannat (1999), Ultramafic exposures and the gravity signature of the lithosphere near the Fifteen-Twenty Fracture Zone (Mid-Atlantic Ridge, 14°–16.5°N), *Earth Planet. Sci. Lett.*, 171, 411–424, doi:10.1016/S0012-821X(99)00169-7.
- Escartin, J., C. Mevel, C. J. MacLeod, and A. M. McCaig (2003), Constraints on deformation conditions and the origin of oceanic detachments: The Mid-Atlantic Ridge core complex at 15°45'N, *Geochem. Geophys. Geosyst.*, 4(8), 1067, doi:10.1029/2002GC000472.
- Escartin, J., D. K. Smith, J. Cann, H. Schouten, C. H. Langmuir, and S. Escrig (2008), Central role of detachment faults in accretion of slow-spreading oceanic lithosphere, *Nature*, 455, 790–794, doi:10.1038/nature07333.
- Farley, K. A., R. A. Wolf, and L. T. Silver (1996), The effects of long alpha-stopping distances on (U-Th)/He ages, *Geochim. Cosmochim. Acta*, 60, 4223–4229, doi:10.1016/S0016-7037(96)00193-7.
- Ferry, J. M., and E. B. Watson (2007), New thermodynamic models and revised calibrations for the Ti-in-zircon and Zr-in-rutile thermometers, *Contrib. Mineral. Petrol.*, 154, 429–437, doi:10.1007/s00410-007-0201-0.
- Foster, D. A., T. M. Harrison, C. F. Miller, and K. A. Howard (1990), 40Ar/39Ar thermochronology of the eastern Mojave Desert, California, and adjacent western Arizona: With implications for the evolution of metamorphic core complexes, *J. Geophys. Res.*, 95, 20,005–20,024, doi:10.1029/JB095iB12p20005.
- Fujiwara, T., J. Lin, T. Matsumoto, P. B. Kelemen, B. E. Tucholke, and J. F. Casey (2003), Crustal Evolution of the Mid-Atlantic Ridge near the Fifteen-Twenty Fracture Zone in the last 5 Ma, *Geochem. Geophys. Geosyst.*, 4(3), 1024, doi:10.1029/2002GC000364.
- Garces, M., and J. S. Gee (2007), Paleomagnetic evidence of large footwall rotations associated with low-angle faults at the Mid-Atlantic Ridge, *Geology*, 35, 279–282, doi:10.1130/G23165A.1.
- Gee, J., and D. Blackman (2004), Lineated near bottom magnetic anomalies over an oceanic core complex, Atlantis Massif (Mid-Atlantic Ridge at 30°N), *Eos Trans. AGU*, 85(17), Jt. Assem. Suppl., Abstract GP31A-15.
- Gee, J., and W. P. Meurer (2002), Slow cooling of middle and lower crust inferred from multicomponent magnetizations of gabbroic rocks from the Mid-Atlantic Ridge south of the Kane fracture zone (MARK) area, *J. Geophys. Res.*, 107(B7), 2137, doi:10.1029/2000JB000062.
- Grimes, C. B., B. E. John, M. J. Cheadle, and J. L. Wooden (2008), Protracted construction of gabbroic crust at a slow-spreading ridge: Constraints from ²⁰⁶Pb/²³⁸U zircon ages from Atlantis Massif and IODP Hole U1309D (30°N, MAR), *Geochem. Geophys. Geosyst.*, 9, Q08012, doi:10.1029/2008GC002063.
- Grimes, C. B., B. E. John, M. J. Cheadle, F. K. Mazdab, J. Wooden, S. Swapp, and J. Schwartz (2009), On the occurrence, trace element geochemistry, and crystallization history of zircon from in situ ocean lithosphere, *Contrib. Mineral. Petrol.*, 158, 757–783, doi:10.1007/s00410-009-0409-2.
- Grimes, C. B., T. Ushikubo, B. E. John, and J. W. Valley (2010), Uniformly mantle-like $\delta^{18}\text{O}$ in zircons from oceanic plagiogranites and gabbros, *Contrib. Mineral. Petrol.*, 161, 13–33, doi:10.1007/s00410-010-0519-x.
- Hansen, L. (2007), Styles of detachment faulting at the Kane Fracture Zone Oceanic Core Complex, 23°N Mid-Atlantic Ridge, master's thesis, Univ. of Wyoming, Laramie, Wyo.
- Ildefonse, B., D. K. Blackman, B. E. John, D. J. Miller, C. J. MacLeod, and the Expedition 304/305 Shipboard Science Party (2007), Oceanic core complexes and crustal accretion at slow-spreading ridges, *Geology*, 35, 623–626, doi:10.1130/G23531A.1.
- John, B. E., and M. J. Cheadle (2010), Deformation and alteration associated with oceanic and continental detachment fault systems: Are they similar?, in *Diversity of Hydrothermal Systems on Slow-Spreading Ocean Ridges*, *Geophys. Monogr. Ser.*, vol. 188, edited by P. Rona et al., pp. 175–205, AGU, Washington D. C.
- John, B. E., and D. A. Foster (1993), Structural and thermal constraints on the initiation angle of detachment faulting in the southern Basin and Range: The Chemehuevi Mountains case study, *Geol. Soc. Am. Bull.*, 105, 1091–1108, doi:10.1130/0016-7606(1993)105<1091:SATCOT>2.3.CO;2.
- John, B. E., D. A. Foster, J. M. Murphy, M. J. Cheadle, A. G. Baines, M. Fanning, and P. Copeland (2004), Determining the cooling history of in situ lower oceanic crust—Atlantis Bank, SW Indian Ridge, *Earth Planet. Sci. Lett.*, 222, 145–160, doi:10.1016/j.epsl.2004.02.014.
- Jöns, N., W. Bach, and T. Schroeder (2009), Formation and alteration of plagiogranites in an ultramafic-hosted detachment fault at the Mid-Atlantic Ridge (ODP Leg 209), *Contrib. Mineral. Petrol.*, 157, 625–639, doi:10.1007/s00410-008-0357-2.
- Karson, J. A. (1999), Geological investigation of a lineated massif at the Kane Transform Fault: Implications for oceanic core complexes, *Philos. Trans. R. Soc. London A*, 357, 713–740, doi:10.1098/rsta.1999.0350.
- Karson, J. A., G. L. Früh-Green, D. S. Kelley, E. A. Williams, D. R. Yoerger, and M. Jakuba (2006), Detachment shear zone of Atlantis Massif core complex, Mid-Atlantic Ridge,



- 30°N, *Geochem. Geophys. Geosyst.*, 7, Q06016, doi:10.1029/2005GC001109.
- Kelemen, P. B., T. Matsumoto, and the Shipboard Scientific Party (1998), Geological results of MODE 98, Leg 1: JAMSTEC/WHOI Shinkai 6500 Cruise to 15°N, Mid-Atlantic Ridge, *Eos Trans. AGU*, 79(45), Fall Meet. Suppl., Abstract U22A-18.
- Kelemen, P. B., et al. (2004), *Proceedings of the Ocean Drilling Program, Initial Reports*, vol. 209, Ocean Drill. Program, College Station, Tex., doi:10.2973/odp.proc.ir.209.2004.
- Kelemen, P. B., E. Kikawa, D. J. Miller, and the Shipboard Scientific Party (2007), Leg 209 summary: Processes in a 20-km-thick conductive boundary layer beneath the Mid-Atlantic Ridge, 14°–16°N, *Proc. Ocean Drill. Program Sci. Results*, 209, 1–33.
- Koepke, J., J. Berndt, S. T. Feig, and F. Holtz (2007), The formation of SiO₂-rich melts within deep oceanic crust by hydrous partial melting of gabbros, *Contrib. Mineral. Petrol.*, 153, 67–84, doi:10.1007/s00410-006-0135-y.
- Kong, L. S., S. C. Solomon, and G. M. Purdy (1992), Micro-earthquake characteristics of a mid-ocean ridge along-axis high, *J. Geophys. Res.*, 97, 1659–1685, doi:10.1029/91JB02566.
- Lagabriele, Y., D. Bideau, M. Cannat, J. A. Karson, and C. Mevel (1998), Ultramafic-mafic plutonic rock suites exposed along the Mid-Atlantic Ridge (10°N–30°N): Symmetrical-asymmetrical distribution and implications for sea-floor spreading processes, in *Faulting and Magmatism at Mid-Ocean Ridges*, *Geophys. Monogr. Ser.*, vol. 106, edited by W. R. Buck, pp. 153–176, AGU, Washington D. C.
- Lavier, L. L., W. R. Buck, and A. N. B. Poliakov (1999), Self-consistent rolling-hinge model for the evolution of large-offset low-angle normal faults, *Geology*, 27, 1127–1130, doi:10.1130/0091-7613(1999)027<1127:SCRHMF>2.3.CO;2.
- Lissenberg, C. J., M. Rioux, N. Shimizu, S. A. Bowring, and C. Mével (2009), Zircon dating of oceanic crustal accretion, *Science*, 323, 1048–1050, doi:10.1126/science.1167330.
- Ludwig, K. R. (2003), User's manual for Isoplot 3.00: A geochronological toolkit for Microsoft Excel, *Spec. Publ.* 4, 70 pp., Berkeley Geochronol. Cent., Berkeley, Calif.
- MacLennan, J., T. Hulme, and S. C. Singh (2005), Cooling of the lower oceanic crust, *Geology*, 33, 357–366, doi:10.1130/G21207.1.
- MacLeod, C. J., et al. (2002), Direct geological evidence for oceanic detachment faulting: The Mid-Atlantic Ridge, 15°45'N, *Geology*, 30, 879–882, doi:10.1130/0091-7613(2002)030<0879:DGEFOD>2.0.CO;2.
- MacLeod, C. J., R. C. Searle, B. J. Murton, J. F. Casey, C. Mallows, S. C. Unsworth, K. L. Achenbach, and M. Harris (2009), Life cycle of oceanic core complexes, *Earth Planet. Sci. Lett.*, 287, 333–344, doi:10.1016/j.epsl.2009.08.016.
- Magde, L. S., A. H. Barclay, D. R. Toomey, R. S. Detrick, and J. A. Collins (2000), Crustal magma plumbing within a segment of the Mid-Atlantic Ridge, 35°N, *Earth Planet. Sci. Lett.*, 175, 55–67, doi:10.1016/S0012-821X(99)00281-2.
- McCaig, A. M., A. Delacour, A. E. Fallick, T. Castelain, and G. L. Fruh-Green (2010), Fluid circulation and isotopic alteration in and beneath oceanic detachment faults in the central Atlantic: Implications for the geometry and evolution of high-temperature hydrothermal circulation cells at slow-spreading ridges, in *Diversity of Hydrothermal Systems on Slow-Spreading Ocean Ridges*, *Geophys. Monogr. Ser.*, vol. 188, edited by P. Rona et al., pp. 207–240, AGU, Washington D. C.
- Mehl, L., and G. Hirth (2008), Plagioclase preferred orientation in layered mylonites: Evaluation of flow laws for the lower crust, *J. Geophys. Res.*, 113, B05202, doi:10.1029/2007JB005075.
- Meurer, W. P., and J. Gee (2002), Evidence for the protracted construction of slow-spread oceanic crust by small magmatic injections, *Earth Planet. Sci. Lett.*, 201, 45–55, doi:10.1016/S0012-821X(02)00660-X.
- Miranda, E. A., and B. E. John (2010), Strain localization along the Atlantis Bank oceanic detachment fault system, Southwest Indian Ridge, *Geochem. Geophys. Geosyst.*, 11, Q04002, doi:10.1029/2009GC002646.
- Morris, A., J. S. Gee, N. Pressling, B. E. John, C. J. MacLeod, C. B. Grimes, and R. C. Searle (2009), Footwall rotation in an oceanic core complex quantified using reoriented Integrated Ocean Drilling Program core samples, *Earth Planet. Sci. Lett.*, 287, 217–228, doi:10.1016/j.epsl.2009.08.007.
- Natland, J. H., P. S. Meyer, H. J. B. Dick, and S. H. Bloomer (1991), Magmatic oxides and sulfides in gabbroic rocks from Hole 735B and the later development of the liquid line of descent, *Proc. Ocean Drill. Program Sci. Results*, 118, 75–111, doi:10.2973/odp.proc.sr.118.163.1991.
- Niu, Y., T. Gilmore, S. Mackie, A. Greig, and W. Bach (2002), Mineral chemistry, whole-rock compositions, and petrogenesis of Leg 176 gabbros: Data and discussion (online), *Proc. Ocean Drill. Program Sci. Results*, 176, 60 pp. (Available at http://www-odp.tamu.edu/publications/176_SR/VOLUME/CHAPTERS/SR176_08.PDF)
- Ogg, J. G., and A. G. Smith (2004), The geomagnetic polarity time scale, in *A Geological Time Scale 2004*, edited by F. M. Gradstein, J. G. Ogg, and A. G. Smith, pp. 63–86, Cambridge Univ. Press, Cambridge, U. K.
- Parrish, R. R., and N. R. Noble (2003), Zircon U-Th-Pb geochronology by isotope dilution—Thermal ionization mass spectrometry (ID-TIMS), in *Zircon, Rev. Mineral. Geochem.*, vol. 53, edited by J. M. Hancher and P. W. O. Hoskin, pp. 182–213, Mineral. Soc. of Am., Washington, D. C.
- Morgan, J. P., and Y. J. Chen (1993), The Genesis of Oceanic Crust: Magma Injection, Hydrothermal Circulation, and Crustal Flow, *J. Geophys. Res.*, 98, 6283–6297, doi:10.1029/92JB02650.
- Reiners, P. W. (2005), Zircon (U-Th)/He thermochronometry, in *Low Temperature Thermochronology: Techniques, Interpretations and Applications*, *Rev. Mineral. Geochem.*, vol. 58, edited P. W. Reiners and T. Ehlers, pp. 151–179, Mineral. Soc. of Am., Washington, D. C.
- Reiners, P. W., T. L. Spell, S. Nicolescu, and K. A. Zanetti (2004), Zircon (U-Th)/He thermochronometry: He diffusion and comparisons with ⁴⁰Ar/³⁹Ar dating, *Geochim. Cosmochim. Acta*, 68, 1857–1887, doi:10.1016/j.gca.2003.10.021.
- Robinson, P. T., J. Erzinger, and R. Emmermann (2002), The composition and origin of igneous and hydrothermal veins in the lower ocean crust—ODP Hole 735B, Southwest Indian Ridge, *Proc. Ocean Drill. Program Sci. Results*, 176, 1–66, doi:10.2973/odp.proc.sr.176.019.2002.
- Rona, P. A., L. Widenfalk, and K. Boström (1987), Serpentinized ultramafics and hydrothermal activity at the Mid-Atlantic Ridge crest near 15°N, *J. Geophys. Res.*, 92, 1417–1427, doi:10.1029/JB092iB02p01417.
- Schroeder, T., and B. E. John (2004), Strain localization on an oceanic detachment fault system, Atlantis Massif, 30°N, Mid-Atlantic Ridge, *Geochem. Geophys. Geosyst.*, 5, Q11007, doi:10.1029/2004GC000728.



- Schroeder, T., M. J. Cheadle, H. J. B. Dick, U. Faul, J. F. Casey, and P. B. Kelemen (2007), Nonvolcanic seafloor spreading and corner-flow rotation accommodated by extensional faulting at 15°N on the Mid-Atlantic Ridge: A structural synthesis of ODP Leg 209, *Geochem. Geophys. Geosyst.*, 8, Q06015, doi:10.1029/2006GC001567.
- Schwartz, J. J., B. E. John, M. J. Cheadle, E. Miranda, C. B. Grimes, J. Wooden, and H. J. B. Dick (2005), Inherited zircon and the magmatic construction of oceanic crust, *Science*, 310, 654–657, doi:10.1126/science.1116349.
- Schwartz, J. J., B. E. John, M. J. Cheadle, P. Reiners, and A. G. Baines (2009), The cooling history of Atlantis Bank oceanic core complex: Evidence for hydrothermal activity 2.6 Myr off-axis, *Geochem. Geophys. Geosyst.*, 10, Q08020, doi:10.1029/2009GC002466.
- Searle, R. C., M. Cannat, K. Fujioka, C. Mevel, H. Fujimoto, A. Bralee, and L. Parson (2003), FUJI Dome; a large detachment fault near 64°E on the very slow-spreading Southwest Indian Ridge, *Geochem. Geophys. Geosyst.*, 4(8), 9105, doi:10.1029/2003GC000519.
- Shen, Y., and D. W. Forsyth (1995), Geochemical constraints on initial and final depths of melting beneath mid-ocean ridges, *J. Geophys. Res.*, 100, 2211–2238, doi:10.1029/94JB02768.
- Singh, S. C., W. C. Crawford, H. Carton, T. Seher, V. Combier, M. Cannat, J. P. Canales, D. Düsünür, J. Escartín, and J. M. Miranda (2006), Discovery of a magma chamber and faults beneath a Mid-Atlantic Ridge hydrothermal field, *Nature*, 442, 1029–1032, doi:10.1038/nature05105.
- Sleep, N. H. (1975), Formation of oceanic crust: Some thermal constraints, *J. Geophys. Res.*, 80, 4037–4042, doi:10.1029/JB080i029p04037.
- Smith, D. K., J. R. Cann, and J. Escartín (2006), Widespread active detachment faulting and core complex formation near 13°N on the Mid-Atlantic Ridge, *Nature*, 442, 440–443, doi:10.1038/nature04950.
- Smith, D. K., J. Escartín, H. Schouten, and J. R. Cann (2008), Fault rotation and core complex formation: Significant processes in seafloor formation at slow-spreading mid-ocean ridges (Mid-Atlantic Ridge, 13°–15°N), *Geochem. Geophys. Geosyst.*, 9(3), Q03003, doi:10.1029/2007GC001699.
- Stacey, J. S., and J. D. Kramers (1975), Approximation of terrestrial lead isotope evolution by a two-stage model, *Earth Planet. Sci. Lett.*, 26, 207–221, doi:10.1016/0012-821X(75)90088-6.
- Stein, C. A., and S. Stein (1992), A model for the global variation in oceanic depth and heat flow with lithospheric age, *Nature*, 359, 123–129, doi:10.1038/359123a0.
- Tarling, D. H. (1983), *Paleomagnetism: Principles and Applications in Geology, Geophysics, and Archaeology*, 379 pp., Chapman and Hall, London.
- Tera, F., and G. J. Wasserburg (1972), U-Th-Pb systematics in three Apollo 14 basalts and the problem of initial Pb in lunar rocks, *Earth Planet. Sci. Lett.*, 14, 281–304, doi:10.1016/0012-821X(72)90128-8.
- Tucholke, B. E., and J. Lin (1994), A geological model for the structure of ridge segments in slow spreading ocean crust, *J. Geophys. Res.*, 99, 11,937–11,958, doi:10.1029/94JB00338.
- Tucholke, B. E., J. Lin, and M. C. Kleinrock (1998), Megamullions and mullion structure defining oceanic metamorphic core complexes on the Mid-Atlantic Ridge, *J. Geophys. Res.*, 103, 9857–9866, doi:10.1029/98JB00167.
- Tucholke, B. E., M. B. Behn, W. R. Buck, and J. Lin (2008), Role of melt supply in oceanic detachment faulting and formation of megamullions, *Geology*, 36, 455–458, doi:10.1130/G24639A.1.
- VanTongeren, J. A., P. B. Kelemen, and K. Hanghoj (2008), Cooling rates in the lower crust of the Oman Ophiolite: Ca in olivine, revisited, *Earth Planet. Sci. Lett.*, 267, 69–82, doi:10.1016/j.epsl.2007.11.034.
- Watson, E. B., and T. M. Harrison (2005), Zircon thermometer reveals minimum melting conditions on earliest Earth, *Science*, 308, 841–844, doi:10.1126/science.1110873.
- Williams, I. S. (1998), U-Th-Pb geochronology by ion microprobe, in *Applications of Microanalytical Techniques to Understanding Mineralizing Processes*, *Rev. Econ. Geol.*, vol. 7, edited by M. A. McKibben, W. C. P. Shanks, and W. I. Ridley, pp. 1–35, Soc. of Econ. Geol., Littleton, Colo.
- Williams, C. M. (2007), Oceanic lithosphere magnetization: Marine magnetic investigations of crustal accretion and tectonic processes in mid-ocean ridge environments, Ph.D. dissertation, Massachusetts Inst. of Technol., Woods Hole Oceanogr. Inst., Cambridge, Mass.
- Wolfe, C. J., G. M. Purdy, D. R. Toomey, and S. C. Solomon (1995), Microearthquake characteristics and crustal velocity structure at 29°N on the Mid-Atlantic Ridge: The architecture of a slow spreading segment, *J. Geophys. Res.*, 100, 24,449–24,472, doi:10.1029/95JB02399.